Late movement of basin-edge lobate scarps on Mercury

E.R. Fegan, D. A. Rothery, S. Marchi, M. Massironi, Susan J. Conway, M. Anand

Late movement of basin-edge lobate scarps on Mercury

Fegan E.R.[1*], Rothery D.A.[1], Marchi S.[2], Massironi M.[3], Conway S.J.[1,4], Anand M.[1,5],

[1]Department of Physical Sciences, The Open University, Walton Hall, Milton Keynes, MK7 6AA, UK. [2]NASA Lunar Science Institute, Southwest Research Institute, Boulder, Colorado 80302, USA. [3]Dipartimento di Geoscienze, Università di Padova, Via Giotto 1, 35137 Padova, Italy. [4]LPG Nantes - UMR CNRS 6112, 2 rue de la Houssinière - BP 92208, 44322 Nantes Cedex 3, France [5]Department of Earth Science, The Natural History Museum, Cromwell Road, London, SW7 5BD, UK.

*Corresponding author (email: emma.fegan@open.ac.uk)

Keywords: Planetary; geology; Mercury; tectonics; model ages; lobate scarps; planetary volcanism.

ABSTRACT

Basin-edge lobate scarps are a sub-type of tectonic shortening structure on the surface of Mercury that have formed at the edge of volcanic units that fill or partly fill impact basins. We have performed a global survey of these features and find that they are widespread in basins across the planet. We obtained model ages from crater size–frequency distribution analysis for a subset of our surveyed basins, for both the smooth plains infill and for the last resolvable tectonic activity on the associated basin-edge scarps. Our results indicate that some of these lobate scarps were still accumulating strain in the late Mansurian (approximately 1 Ga). From a photogeological assessment, we find that the orientations of these basin-edge lobate scarps are similar to those reported for the global population of lobate scarps in earlier studies, appearing to align ~north–south at low latitudes and ~east–west at higher latitudes. However, reassessing these landforms' orientation with artificially illuminated topographic data does not allow us to rule out the effect of illumination bias. We propose that these landforms, the result of crustal shortening in response to global contraction, formed along the interface between the basin floor and the smooth plains unit, which acted as a mechanical discontinuity along which shortening strains were concentrated.

1. INTRODUCTION

Data from the MESSENGER (MErcury Surface, Space ENvironment, GEochemistry, and Ranging) mission flybys and orbital operations have confirmed that tectonic landforms, and shortening structures in particular, are widespread on Mercury's surface (Byrne *et al.*, 2014). Among the most frequently observed features are lobate scarps: curvilinear surface deformations associated with thrust faults, with a steep front scarp and gently dipping back scarp, and topographic relief of hundreds of metres to 1-3 km (Strom, Trask and Guest, 1975; Watters *et al.*, 2002; Solomon, 2011)**.** The generally accepted formation mechanism for the many shortening structures on Mercury, including lobate scarps, is that secular interior cooling and attendant global contraction resulted in thrust faulting in the lithosphere (Strom, Trask and Guest, 1975; Watters, 2004; Byrne *et al.*, 2014).

The distribution and orientation of Mercury's population of shortening structures were detailed by Byrne et al. (2014). In this work we focus on a subset of lobate scarps found at the edges of numerous impact basins (defined here as an impact crater >100 km in diameter), and which can be hundreds of kilometres in length (Rothery and Massironi, 2013). The interiors of these basins are occupied by smooth plains deposits, which are interpreted to be formed due to volcanic infilling; these plains have similar morphological and spectral properties to those of the northern volcanic plains (Denevi *et al.*, 2013; Byrne *et al.*, 2016). The majority of these basin-specific scarps (Byrne et al. 2014) are spatially collocated with the edge of their corresponding basin. Four examples of this feature — which we refer to in this study as "basin-edge scarps" —are illustrated in Figures 1 and 2; an additional example associated with the impact basin Aneirin is shown in Figure 3. They share the morphological features of lobate scarps described above, but follow the edge of the volcanic infill. The vergence of the basin-edge scarps (the facing direction of the steep front scarp, interpreted as the shorter of two limbs of an asymmetric anticline) is always away from the centre of the basin.

Although these features bear a morphological similarity to the steep sides of thick, lobate lava flows within these basins, we interpret these basin-edge scarps as tectonic in nature.

We take this view because basin-filling lavas generally onlap basin walls without discernible relief, and because there are examples of impact craters in the basin fill that have been cut by these scarps (shown in Section 5.2). Moreover, crater areal density measurements at some sites show a resolvable difference in age between the basin fill and a corresponding basin-edge scarp (see section 5.1).

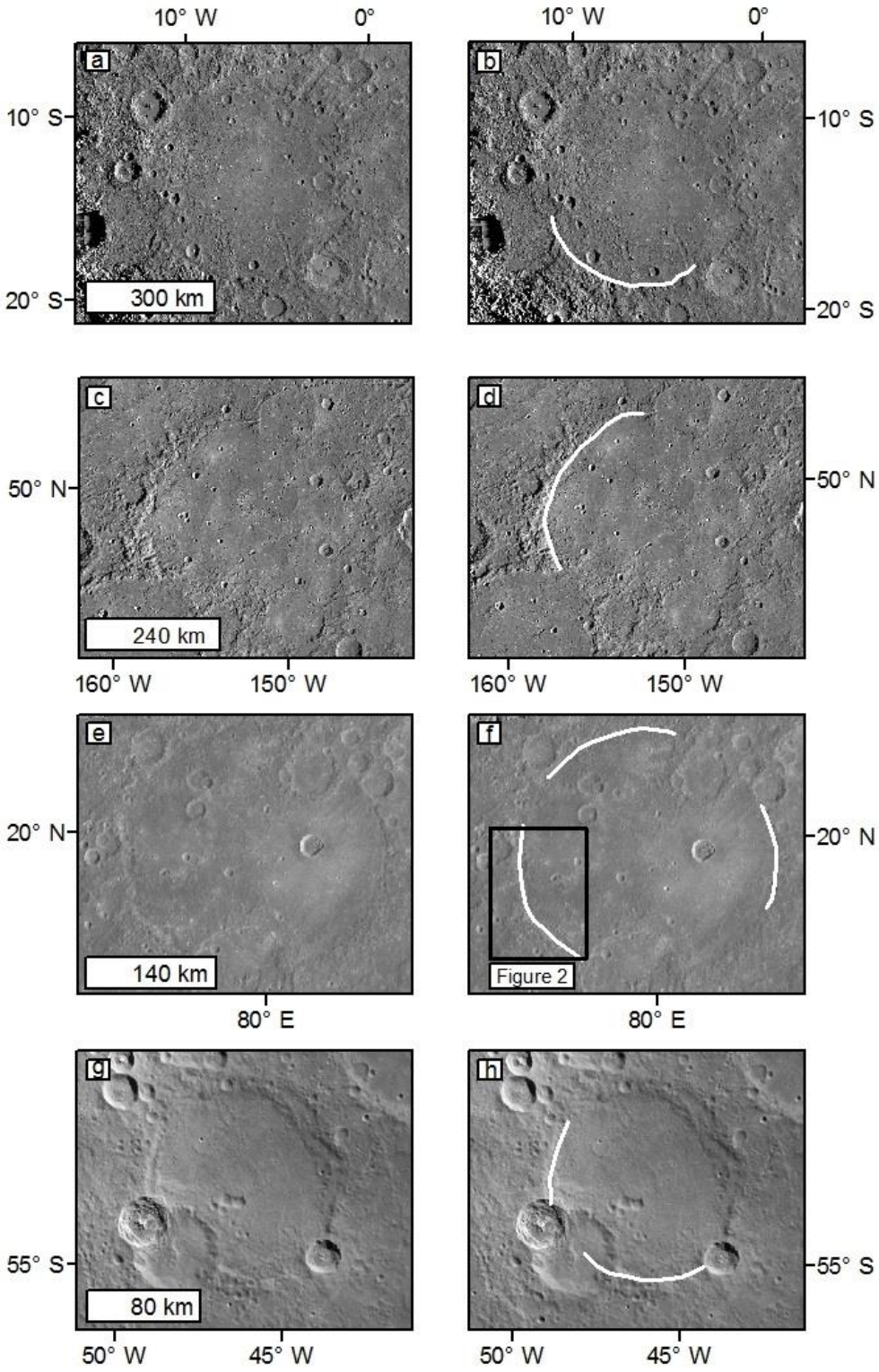

Figure 1: Examples of four basins in which the volcanic infill is part-bounded by one or more lobate scarps. Figure 1 (a) and (b): Sanai (490 km diameter); (c) and (d): Shakespeare (399 km diameter); (e) and (f): Hafiz (280 km diameter); (g) and (h): Shevchenko (143 km diameter).

White lines on (b), (d), (f) and (h) delineate resolvable lobate scarps where basin-fill is thrust towards or over the basin rim. The black rectangle on (f) denotes the area shown in greater detail in Figure 2.

Images are from the MESSENGER MDIS global monochrome base map, which has a resolution of 250 m/px (available: http://messenger.jhuapl.edu/the_mission/mosaics.html).

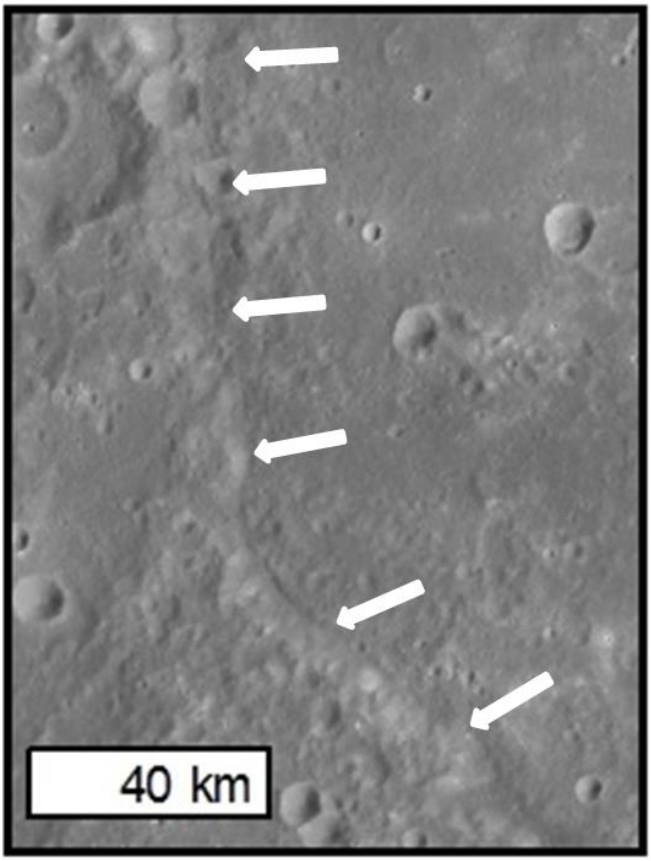

Figure 2: A closer view of a section of the basin-edge scarp of Hafiz basin (as outlined by the back rectangle in Figure 1(f)). The white arrows indicate the basin-edge lobate scarp, and the approximate vergence (i.e. direction of tectonic displacement of the hanging wall).

We conducted a global survey to document the occurrence of scarps at the edges of basin fills. We investigate the distribution of this type of scarp with photogeological mapping, and of both the relative and absolute timing of volcanic infill and scarp formation, using crater size–frequency distribution measurements.

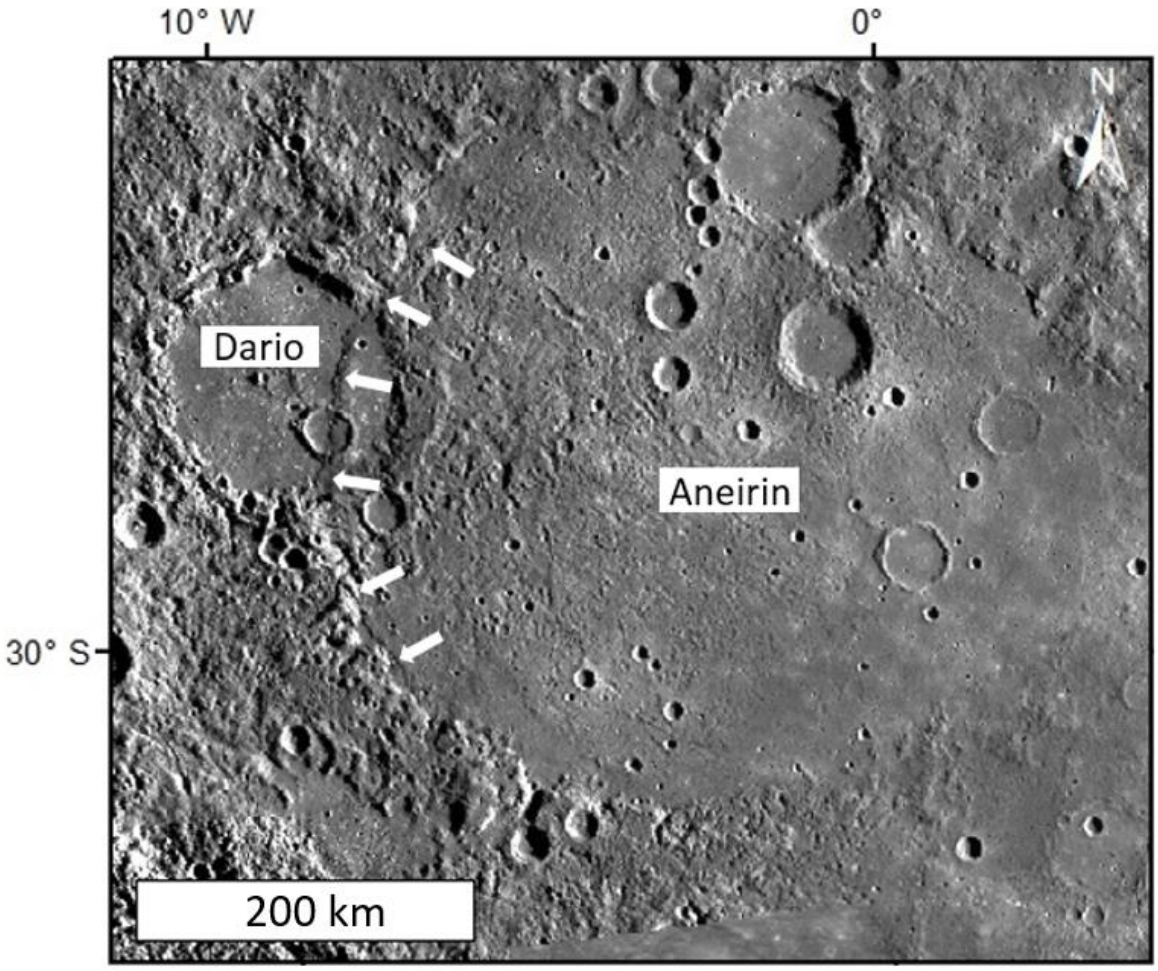

Figure 3: Aneirin basin, and associated basin-edge scarp (indicated by white arrows, which also indicate approximate vergence). The basin-edge scarp of Aneirin cuts through the rim and volcanic infill of the neighbouring younger basin Dario as well as through a still later, unnamed crater inside Dario. Two "ghost craters" can be seen in the east of the smooth plains unit of Aneirin.

2. GLOBAL OCCURENCE OF BASIN-EDGE LOBATE SCARPS

To investigate how common basin-edge scarps are on Mercury, we carried out a global survey with the MESSENGER Dual Imaging Systems (MDIS) (Hawkins *et al.*, 2007) global mosaic (average resolution 250m/pixel). We used the Fassett et al. 2012 database of basins >100 km in diameter, adding basins not included in that study. We then identified all discernible basin-edge lobate scarps within that aggregate population of >100 km diameter basins. Visual examination of each basin in a global database of basins based upon the database of Figure 4 shows the global database of basins examined in this study, all of which have been volcanically filled, and distinguishes those that show evidence for lobate scarps along at least part of the margin of their fill from those that do not. Our survey indicates that basins without basin-edge lobate scarps, have comparable diameters to, and are found in proximity with, those where such scarps are present, indicating that factors other than basin-location and basin-size are involved.

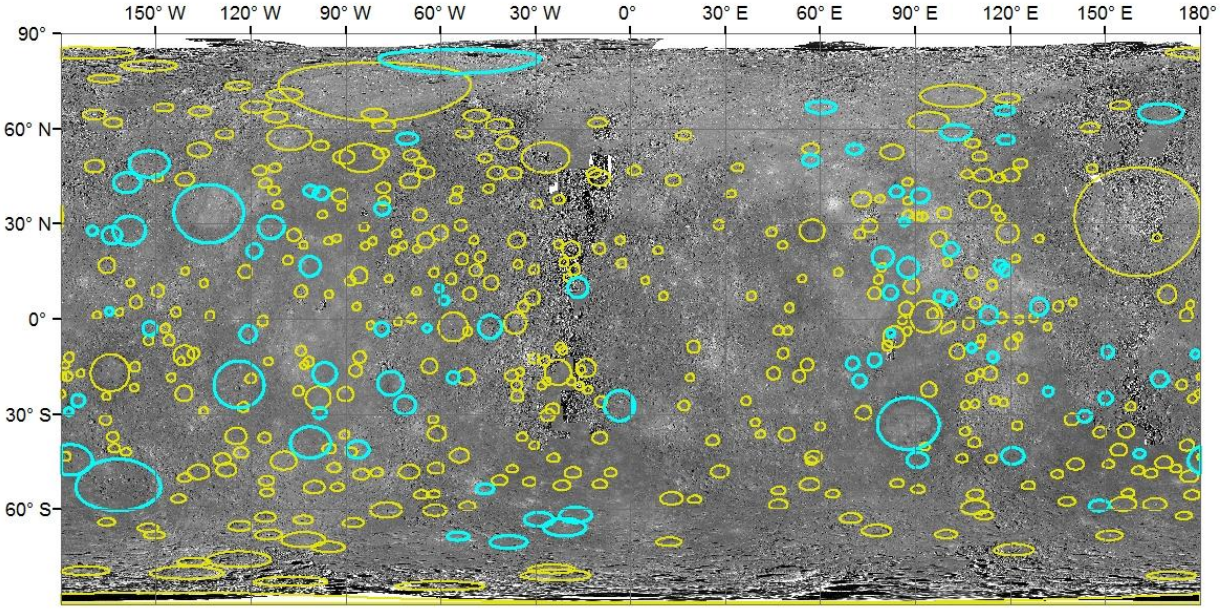

Figure 4: Our photogeological survey results. Basins outlined in yellow have no identifiable lobate scarps at the periphery of their volcanic fills, whereas those outlined in blue have a lobate scarp on some part of the margins of their fill.

4.0 ORIENTATION AND FACING DIRECTIONS

Analysis of shortening structures on Mercury can provide and insight into the global processes responsible for their formation (e.g. Strom et al. 1975, Melosh and McKinnon, 1988, Watters et al., 2009, Byrne et al., 2014). One process proposed to have influenced the tectonic evolution of Mercury is tidal despinning; under this scenario, the decrease in rotationional period, leads to the relaxation of an equatorial tidal bulge (Melosh & Dzurisin 1978; Melosh & McKinnon 1988; Dombard & Hauck 2008; Watters et al. 2015). Despinning has been predicted to form a diagnostic pattern of tectonic features: preferential north–south alignments of shortening structures at low latitudes, and east–west orientations of normal faults at high latitudes (Melosh & McKinnon 1988; Dombard & Hauck 2008; Beuthe 2010).

However, should despinning have operated in combination with global contraction due to secular cooling, which is known to have been extensive on Mercury (Byrne *et al.*, 2014), models have suggested either that north–south aligned thrust faults would be the dominant tectonic structure present (Pechmann and Melosh, 1979; Beuthe, 2010). Alternatively, models that employ a more realistic value for rock strength indicate that north–south-aligned thrust faults would dominantly form at low latitudes with thrust faults with no preferred orientation would preferentially form at higher latitudes (Klimczak, Byrne and Solomon, 2015).

Previous efforts to investigate whether Mercury's lobate scarps display any preferential trend in orientation (e.g., Watters et al. 2009; Di Achille et al. 2012; Byrne et al. 2014) yielded inconclusive results on account of unvarying illumination geometry on the surface resulting in observational bias (Cordell and Strom, 1977). However, Watters et al. (2015) claimed to have identified a definitive orientation preference of structures independent of illumination conditions, with ~north–south orientations (either west- or east-facing) for shortening structures at low latitudes, and ~east–west orientations (either north- or south-facing) at higher latitudes. These results imply that a combination of despinning and global contraction continued until well after the end of the late heavy bombardment of Mercury (Watters *et al.*, 2015), which is thought to have ended by around 3.6–3.9 Ga (Marchi et al.

2013).

Both the orientations and facing direction of the basin-edge lobate scarps we surveyed in this work are shown in Figures 5–7. The data plotted are the frequency of occurrence of lobate scarps per 1° segment of basin circumference (where 0°, i.e., due north, is indicated by a black arrow). For example, Figure 5 indicates a preference for ~east- and ~west-facing directions, and thus a preponderance of ~north–south strikes, for the lobate scarps in our global survey, and in particular a preference for west-facing over east-facing scarps. Note that although this method allows both scarp orientation and facing direction to be displayed, it does not indicate the length of each constituent scarp; for example, scarps that subtend 45° of arc along the circumference of a 100 km-diameter basin and of a 500 km-diameter basin would have necessarily different lengths, but would contribute equally to a plot of this nature.

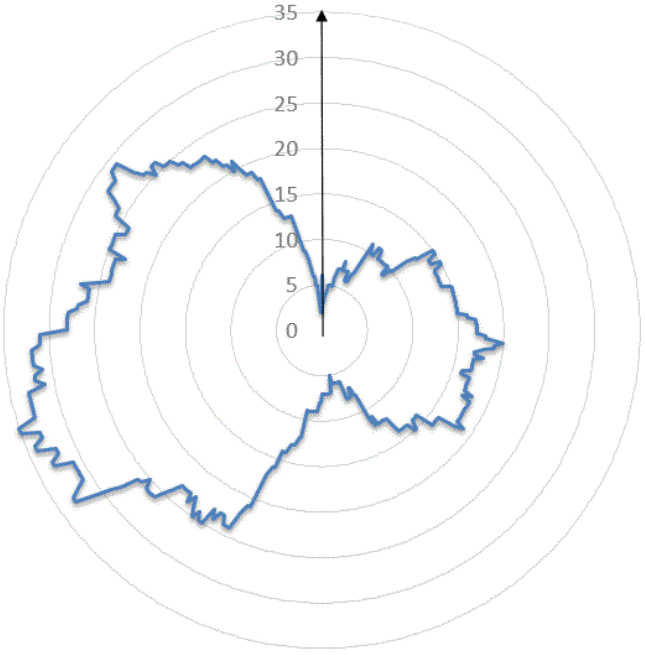

Figure 5: A radial plot displaying the facing directions of the global population of basin-edge scarps (n = 142). The black arrow denotes north; the radial axis indicates frequency of lobate scarp facing direction occurrence (per degree of bearing). This plot indicates a north–south alignment of scarps, which are more commonly west-facing than east-facing.

To test whether or not our results are subject to the same illumination bias suspected in earlier studies, we resurveyed those basin-edge scarps present on shaded-relief models of selected portions of Mercury's surface created from digital terrain models (DTMs). Preusker et al. (2011) produced these DTMs with stereo images from MESSENGER's flybys of

Mercury, and we created shaded-relief models with artificial lighting directions (method as referred to in the supplementary material of Watters et al (2015)). Briefly, we used the Hillshade tool in the Spatial Analyst Toolbox of ArcGIS 10.1 to create two hillshade models with illumination azimuths of 090° and 000°, respectively. The hillshade model with the illumination azimuth of 090° is approximately similar to that of the global monochrome mosaic we carried out our survey on (Section 2), while the illumination azimuth of 000° is perpendicular to the natural illumination in that mosaic (and in all low-Sun images except at polar latitudes).

We found that the preferential orientation results from the radial plots with artificial illumination differed from the results shown in Figure 5. Two examples are shown in Figures 6 and 7 which also show that changing the illumination azimuth resulted in a change of observed preference for facing direction of our surveyed scarps.

Because of this apparent dependence of scarp facing direction (and thus strike) on solar illumination angle, we are unable to discount the influence of illumination geometry on our global survey and scarp orientation results (Figure 5), despite the features involved being several hundred km in length and being relatively easy to identify (as they are, by definition, on the edge of impact basins). Thus, we cannot be certain that basin-edge lobate scarps are preferentially oriented north–south on Mercury.

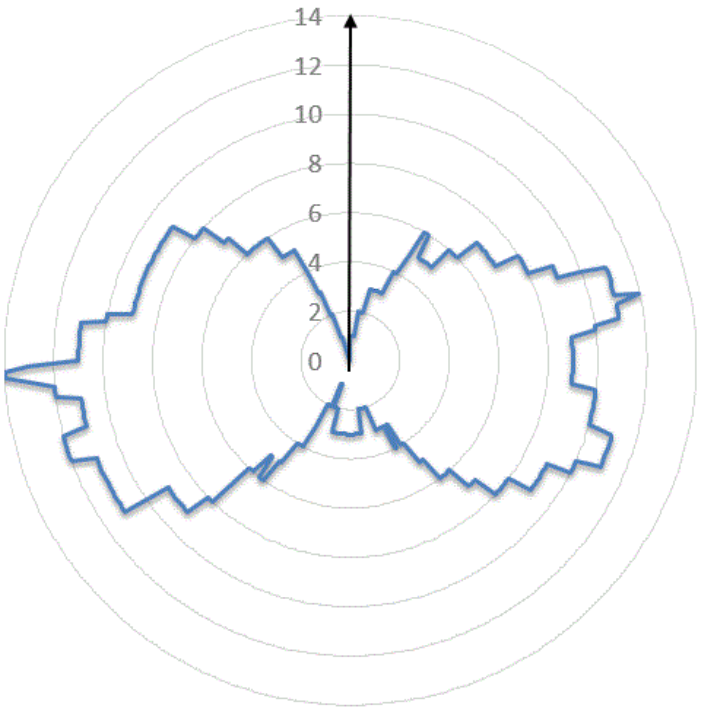

Figure 6: Radial plot of facing directions produced from hillshade models artificially illuminated from the east (n = 40). The scarps show strong preferences for east- or west-facing directions. Note that the total frequency is lower than the global plot (Figure 5) as the DTM we used covers only a portion of the surface.

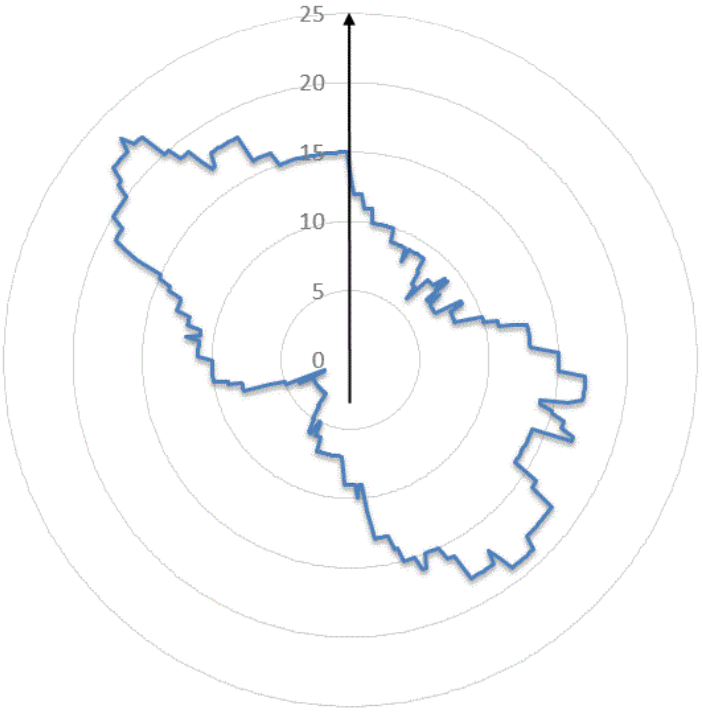

Figure 7: Radial plot of facing directions produced when hillshade model (as used for Figure 6) was artificially illuminated from the north (n = 56), yielding preferential scarp facing directions to the northwest and southeast.

That caveat aside, like Byrne et al. (2014) and Watters et al. (2015), we observe a preference globally for ~north–south orientations of basin-edge lobate scarps (Figure 5), and specifically ~north–south orientations at low latitudes and ~east–west orientations at high latitudes. Byrne et al. (2014) examined the orientation of the global population of shortening structures on Mercury and found them to have ~north–south orientations at low latitudes, and a northeast–southwest trend at higher northern latitudes, but no preferred orientations at high southern latitudes. Our observations agree with this first finding, but not the third (we have not examined the variation of apparent trends with latitude in this study so are unable to comment on the second finding). Klimczak et al. (2015) tested end-member scenarios under which despinning ended prior to the onset of global contraction, or where despinning was still operating when contraction began, and compared their model predictions against the observations of Byrne et al. (2014). Klimczak et al. (2015) concluded, as did Watters et al. (2015), that observational evidence supports a scenario under which despinning was still underway when global contraction began.

5.0 RELATIVE AND ABSOLUTE AGES

5.1 N NUMBERS AND MODEL CRATER RETENTION AGES

To investigate the timing of smooth plains emplacement within basins, and the timing of subsequent basin-edge lobate scarp formation, we conducted a size-frequency distribution (SFD) analysis of a number of smooth plains surfaces both for basins with and without a basin-edge lobate scarp. When identifying craters to produce SFDs for the surface of our selected volcanic fills, we used the highest available resolution MDIS images (which have an average resolution of 50 m/pixel) that cover the count areas. We processed the images with USGS ISIS3 software before importing them into the ArcGIS environment. We determined crater SFDs for these units with CraterTools (Kneissl, van Gasselt and Neukum, 2011) within ArcGIS, digitising primary craters >1 km in diameter. Secondary craters (as identified by clustering, chains and herringbone patterns) were excluded from the counts, although their corresponding areas (accounting for between 0 and 1% of the count areas) were left in. We do not believe removing these areas would have had any impact on our model ages, particularly since we quote them to only two significant figures. The inclusion of craters as small as 1 km in diameter makes it highly likely that secondary craters have been included, despite our efforts to avoid them. However, without including craters down to 1 km in diameter the SFD statistics would have been too unreliable (due to too few craters being included in the counts) to draw any conclusions from.

We selected a subset of eight impact basins >100 km in diameter that have basin-edge lobate scarps for our model age analysis. Note that these eight samples represent approximately 10% of the total population of basin-edge scarps (n = 78), as identified in our survey (see section 2). For comparison, we also determined SFDs for the volcanic fill of eight basins >100 km in diameter that do not have basin-edge scarps. We did so to investigate whether the smooth plains within basins with basin-edge scarps are, in general, older, younger, or comparable in absolute age with the smooth plains within those basins that lack such scarps.

To enable direct comparison between the relative ages of the smooth plains units in Table 2, we calculated the cumulative number of craters equal to or greater than 10 km and 20 km in

287 diameter (N(10) and N(20) respectively) (Arvidson et al. 1979). The smaller the number of
288 superposed craters, the younger the surface is likely to be.
289
290

With basin-edge scarps						Without basin-edge scarps				
Name	**Count Area km^2**	**N(10) (conf. int.)**	**N(20) (conf. int.)**	**Fill (conf. int.) Ga**	**Scarp (conf. int.) Ga**	**Name**	**Count Area km^2**	**N(10) (conf. int.)**	**N(20) (conf. int.)**	**Fill (conf. int.) Ga**
Aneirin	$7.5x10^4$	93 (±35)	27 (±19)	2.2 (±0.3)	0.6 (±0.1)	Mendelson	$4.4x10^4$	45 (±32)	23 (±23)	1.8 (±0.2)
Beethoven	$1.6x10^4$	88 (±23)	31 (±14)	3.5 (±0.1)	1.0 (±0.1)	Hugo	$1.3x10^3$	155 (±109)	N/A	3.7 (±0.1)
Hafiz	$2.1x10^5$	242 (±108)	97 (±69)	2.9 (±0.5)	*1.0 (±0.1)*	Khansa	$4.6x10^3$	N/A	N/A	0.9 (±0.1)
Shakespeare	$7.0x10^4$	72 (±32)	29 (±20)	2.9 (±0.1)	1.0 (±0.1)	Copland	$2.4x10^3$	N/A	N/A	1.7 (±0.4)
Shevchenko	$6.1x10^3$	N/A	N/A	1.5 (±0.2)	1.1 (±0.1)	Unnamed[166°S, 25°W]	$4.0x10^3$	N/A	N/A	3.4 (±0.1)
Unnamed[40°S, 70°W]	$7.5x10^4$	239 (±57)	76 (±32)	3.9 (±0.1)	1.1 (±0.1)	Unnamed[154°N, 67°E]	$3.8x10^3$	261 (±261)	N/A	2.7 (±0.2)
Unnamed[91°N, 38°E]	$1.8x10^4$	N/A	N/A	3.9 (±0.1)	1.1 (±0.1)	Unnamed[69°S, 0°E]	$8.0x10^3$	126 (±126)	N/A	2.4 (±0.3)
Unnamed[150°N, 10°W]	$1.4x10^4$	138 (±97)	N/A	3.0 (±0.3)	1.1 (±0.1)	Unnamed[13°S, 22°W]	$4.2x10^3$	416 (±315)	N/A	2.6 (±0.4)

Table 2: Count areas and N(10) and N(20) numbers for a subset of basins with and without basin-edge scarps . Confidence intervals (conf. int.) are ± one standard deviation, derived as the square root of the number of craters counted, divided by the area over which the count was made, per million square km. Basins where the crater SFD did not include any craters of diameter greater than 10 km or 20 km are indicated by N/A. Columns titled 'Fill (conf. int.)' and 'Scarp (conf. int.)' list our model ages, produced using the Marchi production function (Marchi et al. 2009). Italics indicate poor fits to the data, in which cases the cratering age is highly uncertain as the crater production function does not represent the shape of the cumulative SFD. The unnamed basins are distinguished by the coordinates of their centre points in decimal degrees.

Denevi et al. (2013) published N(10) and N(20) values for the smooth plains within Beethoven basin, one of the basins we examine in this work. They obtained an N(10) value of 82 ±19 and an N(20) value of 32 ±12 for this unit; we obtained N(10) and N(20) values of 88 ±23 and 31 ±14, respectively, for these smooth plains units, in good agreement with the Denevi et al. (2013) values.

Area	N(10) (error)	N(20) (error)
Intercrater plains [1]	217 (±14)	94 (±9)
Caloris interior plains [1]	80 (±7)	26 (±4)
Smooth plains south of Rachmaninoff [1]	58 (±13)	17 (±7)
Northern smooth plains (NSP) [2]	51 (±8) – 81 (±9)	16 (±5) – 30 (±5)
Northern Heavily Catered Terrain (NHCT) [2]	184 (±14) – 256 (±14)	74 (±9) – 122 (±14)

Table 3: N(10) and N(20) values published by previous authors. References: [1]Denevi et al. (2013), [2]Ostrach et al. (2015).

N(10) and N(20) values cannot be used to estimate the last tectonic activity of basin-edge scarps, because N values correspond to the aerial density of impact craters, and provide no absolute age data. To compare the approximate timing of emplacement of the smooth plains units with the age of cessation of resolvable activity on their associated basin-edge scarp, we applied the model production function of Marchi et al. (2009), Massironi et al. (2009), and Marchi et al. (2013) to the crater SFD and buffered SFD data.

To derive relative and absolute model ages on the lobate scarps, which are linear features rather than surface units, we applied the buffered count method (Fassett and Head, 2008), following the example of Giacomini et al. (2015) in applying it to tectonic features.

In this approach, craters that superpose the lobate scarp are counted, except those cut by a clear trace of the scarp —for example, the ~20 km diameter unnamed crater inside Dario in

316 Figure 3 would not be included because the basin-edge scarp of Aneirin cuts straight across
317 it. For a subset of eight of the basin-edge lobate scarps we identified in the survey, we then
318 calculated the feature width (W) by measuring the distance between the base of the front
319 scarp and the base of the back slope (as identified by the break in slope, manifested in
320 image data as a change in shading). Since the lobate scarps also vary in width along their
321 length we took 20–30 measurements at regular intervals and used the mean of these as the
322 value for W for each scarp. For each crater, we measured the diameter (D) and created a
323 buffer around the scarp at a distance S_{Buffer} (using ArcGIS 10.1). The areas of these buffers
324 were then used in the crater statistics calculations, and were calculated as follows:
325

326 $$S_{Buffer} = 1.5\,D + 0.5\,W \quad (1)$$

327

328 Since the buffered method was not initially designed to be used on tectonic features, the
329 following points should be borne in mind:

330 - The method includes craters that are not directly superposed onto the structure of
331 interest (although their ejecta is superposed onto the structure).
332 - Faults are frequently composed of segments on which discrete slip events can occur,
333 and so obtaining a single model age for the cessation of activity along the aggregate
334 structure is an oversimplification.
335 - The count areas involved in linear features (as described above) are necessarily
336 small, which can result in large errors from small-number statistics.

337 It is important to note that this buffered method provides an estimate for the age of
338 cessation of resolvable activity on the scarp. Due to likely fault reactivation, it is not possible
339 to use this method to determine the time at which faulting began.
340

341 Marchi et al. (2013) defined the terms “hard rock” and “cohesive soil” to characterise two
342 end-member target properties, the choice of which changes the applicable production
343 function. Here, we followed the example of Giacomini et al. (2015) in regarding the former
344 term to mean unfractured rock and the latter to denote rock with reduced strength due to
345 fracturing. The Marchi et al. (2009) MPF also accommodated rheological layering of the

target material, if observations of the surface or crater SFD data support the possibility of crustal layering (Marchi *et al.*, 2011; Ferrari *et al.*, 2015). To facilitate comparison between data obtained for the basins in Table 2, we consistently applied the following parameters: hard rock scaling (tensile strength: 2 x 10^8 dyne cm^{-2}) with no rheological layering and with predominantly Near-Earth Object population of impactors.

Along with our areal crater density values, we present our model age results in Table 2; plots for the volcanic infill of Shakespeare basin, and associated basin-edge scarp, using the Marchi et al. (2009) MPF are shown in Figure 8. Plots for the other results in Table 2 are given as supplementary material. The errors in Table 2 result from the process of fitting a production function to the cumulative SFD data only and do not include methodological errors involved in crater SFD analysis (such as those set out above).

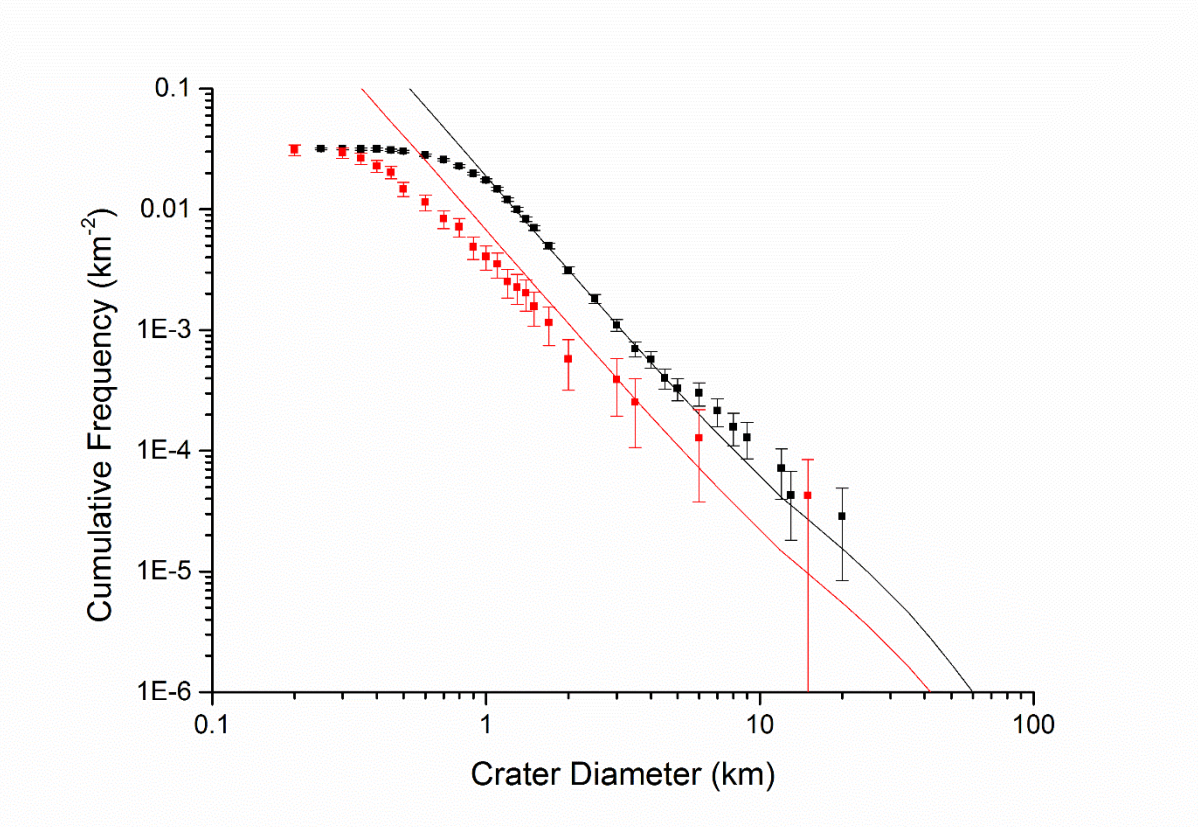

Figure 8: Marchi production function model age plots for the volcanic fill (black) and basin-edge scarp (red) of Shakespeare.

The absolute model ages derived by consistent application of the Marchi et al. (2009) MPF (Table 2) for the volcanic infills in the basins of this study with basin-edge scarps suggest a

range of model ages for this last volcanic activity between 1.5 and 3.9 Ga. For the basins without basin-edge scarps, we obtained absolute model ages ranging from 0.9 Ga to 3.7 Ga. The sample size is small —eight basins with basin-edge scarps and eight basins without such structures— but our data indicate a range of ages for smooth plains units, whether or not they have basin-edge scarps. Our N(10) and N(20) values for Aneirin and Beethoven are the same, within error, to values recently found by Byrne et al. (2016). Byrne et al. (2016) derived an N(10) value for Aneirin of 72 ± 20 (our value: 93 ± 35), an N(20) value of 22 ± 11 (our value: 27 ± 19), and for Beethoven an N(10) value of 92 ± 22 (our value: 88 ± 23) and an N(20) value of 31 ± 13 (our value: 31 ± 14). Our absolute model ages for the smooth plains units of these two basins differ, however, from those of Byrne et al. (2016), who applied a different MPF (that of Le Feuvre & Wieczorek (2011)) and obtained absolute model ages of ~3.7/3.8 Ga for both smooth plains units using porous scaling. When they used non-porous scaling, Byrne et al. (2016) obtained ages of ~2.2 Ga (Aneirin) and 2.7 Ga (Beethoven) which are comparable to our absolute ages but the errors for the non-porous scaling fits were of the order of several billion years.

Comparison between the model ages for the tectonic landforms and the smooth plains indicates that the application of the buffered method to linear tectonic features, as opposed to the Martian valley floors for which it was designed, produces results consistent with the stratigraphic observation that the last tectonic activity on the basin-edge scarps post-dates the emplacement of the most recent volcanic infill. This comparison is also consistent with new evidence of recent tectonic activity in the form of detection of small scale and necessarily young thrust scarps during MESSENGER's end-of-mission low altitude campaign (Watters et al., 2016).

Our results also indicate that the interval between the smooth plains emplacement and the last discernible movement on the associated basin-edge lobate scarp usually exceeds 1 Ga. The absolute model ages for the last resolvable slip on the basin-edge lobate scarps are clustered around approximately 1 Ga (with a range of 0.6 to 1.1 Ga). Giacomini et al. (2015) suggested that activity on small scarp segments or small individual scarps continued, perhaps even to the present, having found that buffer-derived model ages for a ~2000 km-long thrust system (composed of multiple lobate scarps 100 – 350 km in length), the "Blossom thrust system", indicated that these structures were most active prior to 3.5 Ga

(Model ages in this case were produced under the assumption of a layered target with cohesive soil on top of hard rock, which we note is likely to produce generally older results than the uniform hard rock composition of the target body in the model ages we present). Our results suggest that activity continued on the subset of lobate scarps that we investigate here until considerably more recently than 3.5 Ga.

5.2 Verification of the Mansurian age of basin-edge scarps

Because the MPF model ages for the basin-edge scarps in Table 2 extend well into the Mansurian, we examined these structures in more detail with high-resolution MDIS images. Our aim was to determine whether any craters cross-cut by the lobate scarps appear themselves to be Mansurian in age, in order to provide additional evidence to support our inference that the formation of basin-edge scarps was indeed still occurring during the Mansurian (Table 1). The Mansurian epoch is now considered to extend from 1.9–0.3 Ga (Banks et al. 2016). Using the established method for estimating age of Hermean craters on the basis of their degradation state (Spudis and Guest, 1988), we searched for the presence of morphologically crisp rims, visible terracing within a given crater, a visible central peak, and a visible ejecta blanket (with or without rays) . Using the global MDIS mosaic basemap we identified three craters that match the above morphological requirements and that are crosscut by basin-edge scarps. We then examined these craters with higher resolution (average 50 m/pixel) MDIS images (Figures 9a–c).

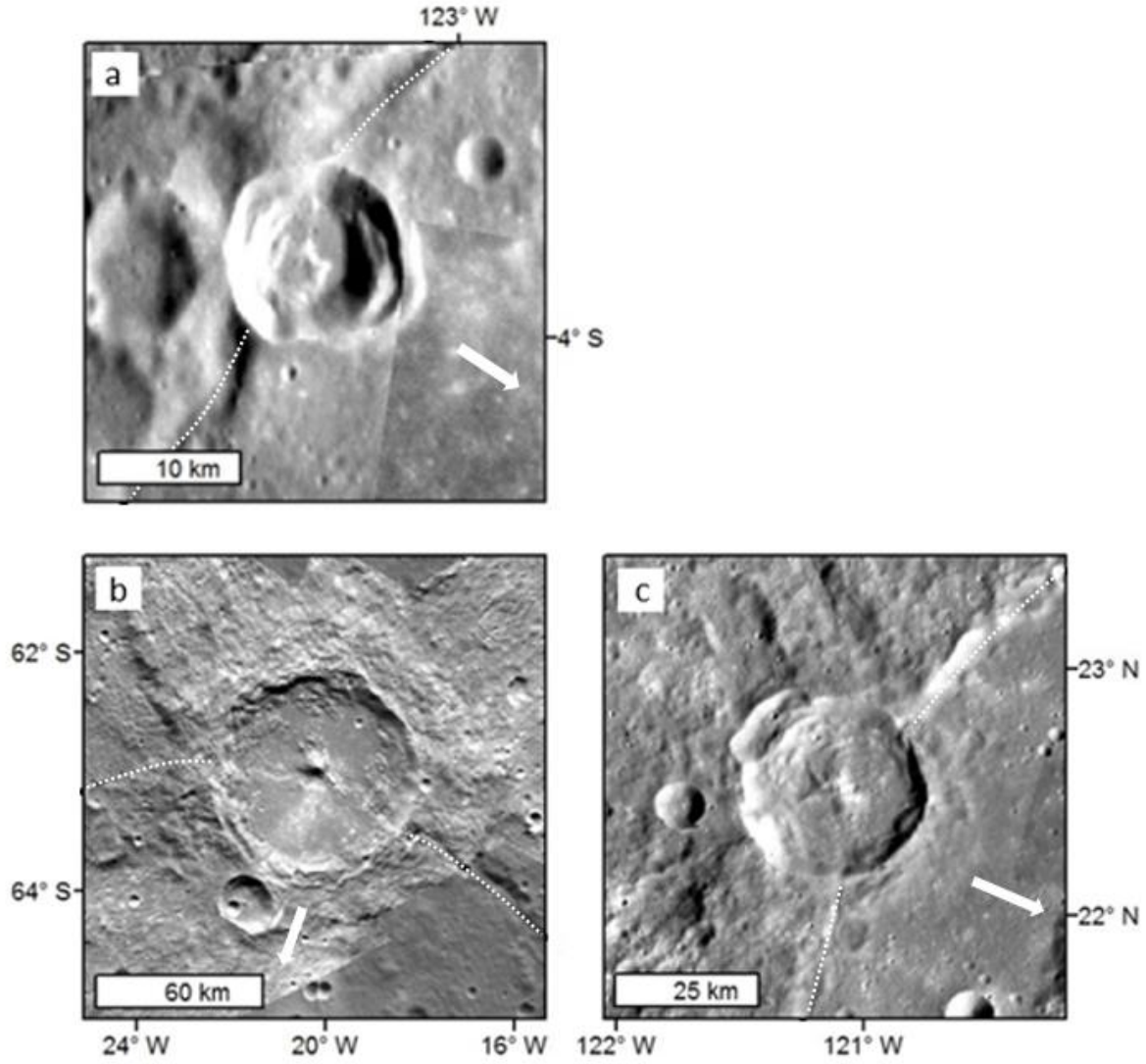

Figure 9 (a–c): Three examples of craters, assessed to have formed during the Mansurian on the basis of degradation state, which are cut and deformed by basin-edge scarps. The white dotted lines indicate the basin-edge scarp (delineated only outside the cross-cut craters to avoid obscuring detail), and the white arrows indicate the direction to the centre of the volcanically infilled basin in each case. The volcanically infilled basins in each case are: (a) Unnamed (centre coordinates: 04°S, 123°W), 14 km diameter (images: EN1051949290M and EN0257562458M), (b) Pushkin (the crater that has been cut through by the basin-edge lobate scarp is Tsurayuki, 83 km diameter) (images: EN1066019121M, EN1066078737M and EN1066019149M), and (c) Durer, 31 km diameter (images: EN0211806621M, EN0227048749M and EN0211806621M).

In the case of Figure 9a, the unnamed crater centred at 04°S, 123°W, there are subtle morphological indications that the scarp affects at least the northern rim, but the evidence for tectonic deformation here is equivocal. However, the craters in Figures 9b and c are

definitely cut by their proximal basin-edge lobate scarps, as the trace of the scarp can be seen on both the crater floor and in the crater wall.

Our observations of craters we assess as Mansurian on the basis of their morphology that are cross-cut by basin-edge lobate scarps supports our model ages results (Table 2), since they also indicate tectonic activity was occurring along these structures after the emplacement of the volcanic infill (in the Mansurian or possibly Kuiperian epoch).

6. DISCUSSION

6.1 PROPOSED FORMATION MECHANISM

Upon the basis of the location and morphology of the basin-edge lobate scarps, we propose the following formation sequence (depicted in Figure 10):

1. An impact event creates a basin.
2. Regolith accumulates on the basin floor.
3. This basin is subsequently flooded by basaltic lavas that solidify to form a "smooth plains" unit (Strom, Trask and Guest, 1975; Denevi *et al.*, 2013). The interface between the basin floor and the base of the smooth plains unit may represent a mechanical discontinuity, especially if there had been time for an appreciable thickness of regolith to develop prior to flooding. The expectation is that regolith growth on Mercury is faster than on the Moon, since the median impact velocity at Mercury is approximately double that at the Moon (because Mercury is deeper in the Sun's gravity well (Langevin, 1997)). The observation of "ghost craters" visible within some of the smooth plains units (for example, Aneirin shown in Figure 3) indicates that a substantial period of time elapsed between basin creation and the most recent episode of volcanic plains emplacement in at least some cases (cf. Byrne et al. 2016).
4. As Mercury's crust shortens due to global contraction, fault nucleation occurs along the mechanically weak interface, and propagates along it before breaching the surface at the edge of the basin infill. The mechanically weak interface is at shallow crustal levels, where fault nucleation is most favourable within a stress field driving

457 global contraction (Klimczak, 2015). A detachment fault, along which the overlying
458 material slides, forms along the interface.
459 5. The smooth plains unit moves along the detachment fault, essentially as a hanging
460 wall block, forming an arcuate lobate scarp (or scarps, since we observed examples
461 where a basin-edge scarp has formed at opposite edges of the same volcanically
462 filled basin) at the basin margin that approximately follows the inner edge of the
463 original impact basin rim and, with increased amounts of shortening strains, over-
464 thrusts it.

465 The mechanism we propose is comparable, although smaller in scale, to the basal
466 décollement proposed by Rothery & Massironi (2010) beneath Beagle Rupes. Mechanical
467 discontinuities within the crust of Mercury that have been suggested by Byrne et al. (2014)
468 and hypothesised to be a contributing factor in the formation of Discovery and Adventure–
469 Resolution Rupes (Watters et al. 2001). We observe that basin-edge scarps' vergence is
470 always outwards facing, and that the scarps themselves follow the interior rim of the
471 original basin without extending beyond it (except in examples where the smooth plains
472 unit has overthrust the original rim). The mechanism we propose here accounts for these
473 observations. When crustal shortening is localised along the interface between the basin
474 floor and the base of the smooth plain infill (with a buried layer of regolith at some depth
475 possibly also contributing, as discussed in point 3, above), that interface could constitute a
476 detachment surface that would act as a stress guide into which thrust faults would be
477 channelled (Zoback, Townend and Grollimund, 2002). The smooth plains unit within the
478 original basin is not fractured in this scenario, but instead is forced upwards along the
479 detachment fault towards the rim of the original impact basin.

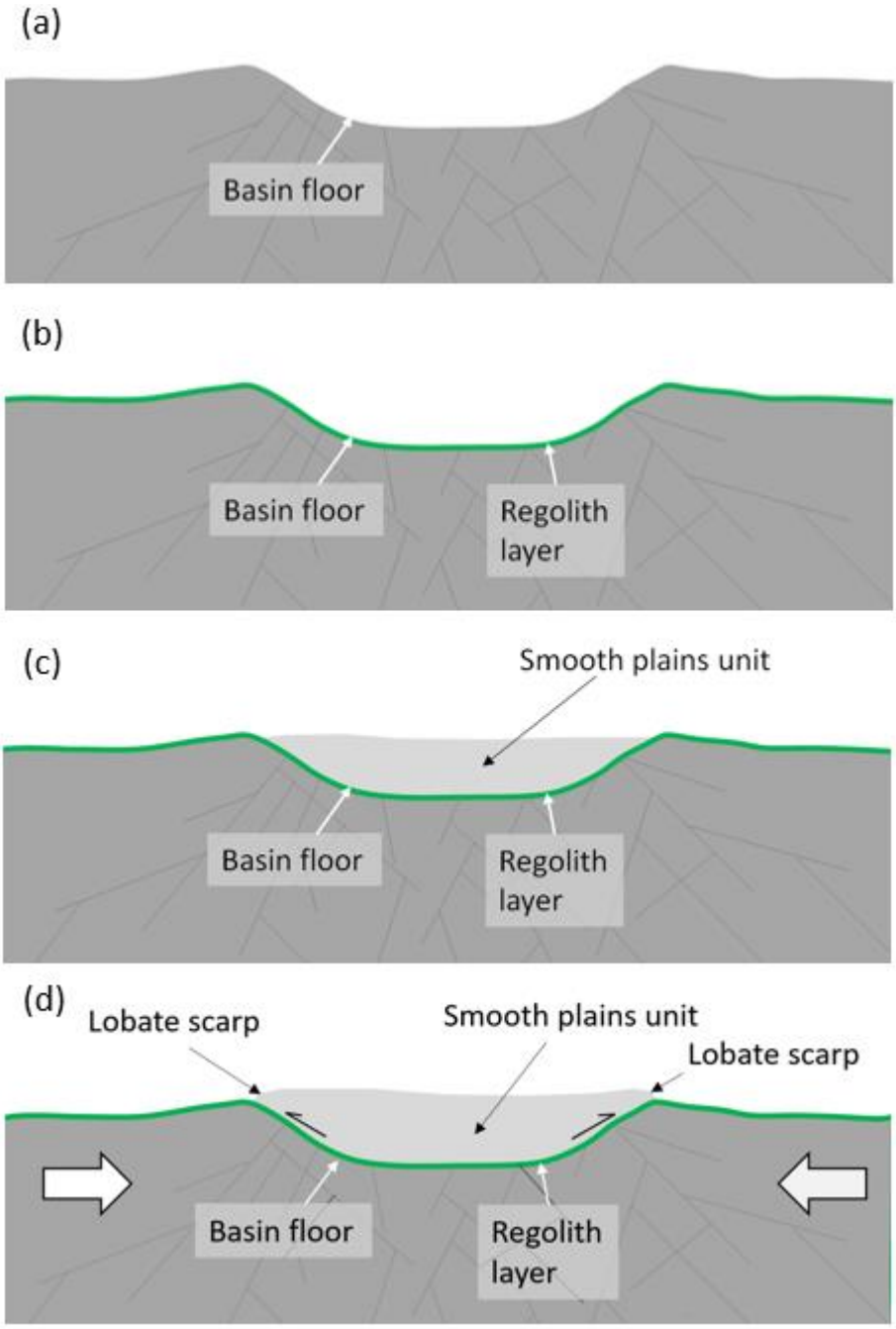

Figure 10: Cartoon depicting the basin-edge lobate scarp formation mechanism that we propose here. (a) The formation of an impact basin results in fracturing of the crust below and surrounding the impact basin (indicated by fine black lines). (b) A layer of regolith forms through continued impact bombardment (shown in green). (c) The basin is infilled by lava. (d) The large white arrows indicate direction of maximum compressive stresses in the lithosphere; as the crust is shortened, a fault (or faults) nucleate along the plane of weakness, resulting in movement along the interface between the basin floor and the base of the smooth plains unit. The example above depicts a basin with two lobate scarps (in this cross-sectional diagram: left and right). The cartoons are not to scale.

6.2 TIMING AND LOCATIONS OF FORMATION

Volcanic activity on a very large scale (for example the northern volcanic plains and Caloris Plainitia) ended on Mercury by around 3.5 Ga (Byrne et al. 2016) with only smaller-scale volcanic flooding continuing thereafter (Prockter *et al.*, 2010; Marchi *et al.*, 2011; Byrne *et*

515 *al.*, 2016). Our results indicate that volcanism of sufficient scale to cover basin floors of
516 approximate areas of 8 x 10^4 km^2 (for basins with a diameter of 100 km) and above
517 continued until at least approximately 1.5 Ga. Our youngest example (according to the
518 model ages we calculated: see Table 2) with a basin-edge scarp is Shevchenko (1.5 ±0.2 Ga),
519 and our youngest example without a basin-edge scarp is Khansa (0.9 ±0.1 Ga). These results
520 are consistent with the findings of Marchi et al. (2011), who derived ages younger than ~1.0
521 Ga for the smooth plains fill of two basins (Raditladi and Rachmaninoff), though it is likely
522 the fill in at least one of those cases is impact melt rather than volcanic lavas (Blair *et al.*,
523 2013). The ascent of magma is assisted by the fracturing created by impacts (Melosh, 2011;
524 Klimczak, 2015; Byrne *et al.*, 2016) potentially accounting for how relatively large volcanic
525 plains formed so late in Mercury's history despite ongoing global contraction.

526 The model ages we determined for the basin-edge lobate scarps lie between 0.6 and 1.1 Ga
527 and they average to approximately 1 Ga (see Table 2). Under a scenario in which sufficient
528 time elapsed between basin formation and volcanic infilling for a regolith to form on the
529 original basin floor, then the presence of this regolith layer could constitute a detachment
530 surface (Zoback, Townend and Grollimund, 2002). However, although model age difference
531 between basin formation and the youngest lava infill can sometimes be resolved (Marchi *et*
532 *al.*, 2011; Ferrari *et al.*, 2015) it is not possible to determine the interval between the basin-
533 forming impact and emplacement of the first volcanic fill, and therefore it is not possible to
534 determine whether or not there was time for a sufficient thickness of regolith to form.
535 However, we have observed several instances of ghost craters, such as those visible in
536 Figure 3. The presence of these landforms suggests a significant time interval during which
537 regolith could form, contributing themselves to the growth of regolith by way of their ejecta
538 blankets.

539

540 **7. CONCLUSIONS**

541 Our results suggest that:

542 - Effusive volcanism of sufficient volume to extend across the floors of basins 100 km
543 in diameter or greater continued until at least early Mansurian (approximately 1.5

Ga), possibly assisted by impact fracturing that allowed this relatively late ascent of magma to the surface despite Mercury's history of sustained global contraction.

- The use of the buffered method on tectonic features produces results consistent with the observed stratigraphy (Byrne *et al.*, 2016).
- Resolvable deformation accommodated by basin-edge lobate scarps appears to have ceased between ~1.1 Ga and ~0.6 Ga, in the mid-to-late Mansurian, at least as determined with our crater areal density surveys and our model ages.
- We suggest that the interface between the original basin floor and the base of the smooth plains units acts as a mechanical discontinuity along which detachment faulting could have occurred.

With regard to the orientation of basin-related lobate scarps we note that the results of our global survey are to first order, consistent with those of Watters et al. (2015) and Byrne et al. (2014), since we also observe a preference for north–south orientations at low latitudes and east–west at higher latitudes. However, our conclusions differ from those of Watters et al. (2015) since we found that the orientation/facing direction plots for structures in those same areas do not consistently show these preferences when the illumination direction is artificially varied. This strongly indicates to us that lighting bias cannot be ruled out when a north–south preference in orientation is detected on the surface of Mercury, as has been proposed by Byrne et al. (2014) and Klimczak et al. (2015).

Acknowledgements: We thank Paul Byrne and Christian Klimczak for undertaking substantial reviews of this manuscript. Additional thanks due to Thomas Barrett for his assistance creating figures used in the manuscript and supplementary material. This work was funded by a Science and Technology Facilities Council (SFTC) studentship to ERF, STFC grants (ST/L000776/1) to MA and (ST/N0039X/1 and ST/M002101/1) to DAR.

REFERENCES

Arvidson, R., Boyce, J., Chapman, C., Cintala, M., Fulchignoni, M., Moore, H., Neukum, G., Schultz, P., Soderblom, L., Strom, R., Woronow, A. and Young, R. (1979) 'Standard Techniques for Presentation and Analysis of Crater Size-Frequency Data', *Icarus*, 474, pp. 467–474.

Banks, M. E., Xiao, Z., Braden, S. E., Marchi, S., Chapman, C. R., Barlow, N. G. and Fassett, C. I. (2016) 'Revised age constraints for Mercury's Kuiperian and Mansurian systems', *LPSC 47*, 2943.

Beuthe, M. (2010) 'East–west faults due to planetary contraction', *Icarus*, 209(2), pp. 795–817. doi: 10.1016/j.icarus.2010.04.019.

Blair, D. M., Freed, A. M., Byrne, P. K., Klimczak, C., Prockter, L. M., Ernst, C. M., Solomon, S. C., Melosh, H. J. and Zuber, M. T. (2013) 'The origin of graben and ridges in Rachmaninoff, Raditladi, and Mozart basins, Mercury', *Journal of Geophysical Research: Planets*, 118(1), pp. 47–58. doi: 10.1029/2012JE004198.

Byrne, P. K., Klimczak, C., Şengör, A. M. C., Solomon, S. C., Watters, T. R. and Hauck, S. A. (2014) 'Mercury's global contraction much greater than earlier estimates', *Nature Geoscience*, 7(April), pp. 301–307. doi: 10.1038/NGEO2097.

Byrne, P. K., Ostrach, L. R., Fassett, C. I., Chapman, C. R., Denevi, B. W., Evans, A. J., Klimczak, C., Banks, M. E. and Head, J. W. (no date) 'Widespread effusive volcanism on Mercury ended by about 3.6 Ga', *Geophysical Research Letters*.

Byrne, P. K., Ostrach, L. R., Fassett, C. I., Chapman, C. R., Denevi, B. W., Evans, A. J., Klimczak, C., Banks, M. E., Head, J. W. and Solomon, S. C. (2016) 'Widespread effusive volcanism on Mercury likely ended by about 3.5 Ga', *Geophysical Research Letters*, pp. 7408–7416. doi: 10.1002/2016GL069412.Received.

Cordell, B. M. and Strom, R. G. (1977) 'Global tectonics of Mercury and the moon', *Physics of the Earth and Planetary Interiors*, 15(2–3), pp. 146–155. doi: 10.1016/0031-9201(77)90027-9.

602 Denevi, B. W., Ernst, C. M., Meyer, H. M., Robinson, M. S., Murchie, S. L., Whitten, J. L.,
603 Head, J. W., Watters, T. R., Solomon, S. C., Ostrach, L. R., Chapman, C. R., Byrne, P. K.,
604 Klimczak, C. and Peplowski, P. N. (2013) 'The distribution and origin of smooth plains on
605 Mercury', *Journal of Geophysical Research: Planets*, 118(5), pp. 891–907. doi:
606 10.1002/jgre.20075.

607 Dombard, A. J. and Hauck, S. a. (2008) 'Despinning plus global contraction and the
608 orientation of lobate scarps on Mercury: Predictions for MESSENGER', *Icarus*. Elsevier Inc.,
609 198(1), pp. 274–276. doi: 10.1016/j.icarus.2008.06.008.

610 Fassett, C. I., Head, J. W., Baker, D. M. H., Zuber, M. T., Smith, D. E., Neumann, G. a.,
611 Solomon, S. C., Klimczak, C., Strom, R. G., Chapman, C. R., Prockter, L. M., Phillips, R. J.,
612 Oberst, J. and Preusker, F. (2012) 'Large impact basins on Mercury: Global distribution,
613 characteristics, and modification history from MESSENGER orbital data', *Journal of*
614 *Geophysical Research: Planets*, 117(E12), p. n/a-n/a. doi: 10.1029/2012JE004154.

615 Ferrari, S., Massironi, M., Marchi, S. and Cremonese, G. (2015) 'Age relationships of the
616 Rembrandt basin and Enterprise Rupes , Mercury', in Platz, T., Massironi, M., Byrne, P. K.,
617 and Hiesinger, H. (eds) *Volcanism and Tectonism Across the Inner Solar System*. Geological
618 Society, London, Special Publications, pp. 159–172. doi: 10.1144/SP401.20.

619 Le Feuvre, M. and Wieczorek, M. A. (2011) 'Nonuniform cratering of the Moon and a revised
620 crater chronology of the inner Solar System', *Icarus*. Elsevier Inc., 214(1), pp. 1–20. doi:
621 10.1016/j.icarus.2011.03.010.

622 Hawkins, S. E., Boldt, J. D., Darlington, E. H., Espiritu, R., Gold, R. E., Gotwols, B., Grey, M. P.,
623 Hash, C. D., Hayes, J. R., Jaskulek, S. E., Kardian, C. J., Keller, M. R., Malaret, E. R., Murchie, S.
624 L., Murphy, P. K., Peacock, K., Prockter, L. M., Reiter, R. A., Robinson, M. S., Schaefer, E. D.,
625 Shelton, R. G., Sterner, R. E., Taylor, H. W., Watters, T. R. and Williams, B. D. (2007) 'The
626 Mercury Dual Imaging System on the MESSENGER Spacecraft', *Space Science Reviews*,
627 131(1–4), pp. 247–338. doi: 10.1007/s11214-007-9266-3.

628 Klimczak, C. (2015) 'Limits on the brittle strength of planetary lithospheres undergoing
629 global contraction', *Journal of Geophysical Research : Planets*, pp. 2135–2151. doi:
630 10.1002/2015JE004851.

631 Klimczak, C., Byrne, P. K. and Solomon, S. C. (2015) 'A rock-mechanical assessment of
632 Mercury's global tectonic fabric', *Earth and Planetary Science Letters*. Elsevier B.V., 416, pp.
633 82–90. doi: 10.1016/j.epsl.2015.02.003.

634 Kneissl, T., van Gasselt, S. and Neukum, G. (2011) 'Map-projection-independent crater size-
635 frequency determination in GIS environments—New software tool for ArcGIS', *Planetary
636 and Space Science*. Elsevier, 59(11–12), pp. 1243–1254. doi: 10.1016/j.pss.2010.03.015.

637 Langevin, Y. (1997) 'The regolith of Mercury: present knowledge and implications for the
638 Mercury Orbiter mission', *Planetary and Space Science*, 45(1), pp. 31–37. doi:
639 10.1016/S0032-0633(96)00098-0.

640 Marchi, S., Bottke, W. F., Cohen, B. A., Wünnemann, K., Kring, D. A., McSween, H. Y., De
641 Sanctis, M. C., O'Brien, D. P., Schenk, P., Raymond, C. A. and Russell, C. T. (2013) 'High-
642 velocity collisions from the lunar cataclysm recorded in asteroidal meteorites', *Nature
643 Geoscience*. Nature Publishing Group, 6(4), pp. 303–307. doi: 10.1038/ngeo1769.

644 Marchi, S., Chapman, C. R., Fassett, C. I., Head, J. W., Bottke, W. F. and Strom, R. G. (2013)
645 'Global resurfacing of Mercury 4.0-4.1 billion years ago by heavy bombardment and
646 volcanism.', *Nature*, 499(7456), pp. 59–61. doi: 10.1038/nature12280.

647 Marchi, S., Massironi, M., Cremonese, G., Martellato, E., Giacomini, L. and Prockter, L.
648 (2011) 'The effects of the target material properties and layering on the crater chronology:
649 The case of Raditladi and Rachmaninoff basins on Mercury', *Planetary and Space Science*.
650 Elsevier, 59(15), pp. 1968–1980. doi: 10.1016/j.pss.2011.06.007.

651 Marchi, S., Mottola, S., Cremonese, G., Massironi, M. and Martellato, E. (2009) 'a New
652 Chronology for the Moon and Mercury', *The Astronomical Journal*, 137(6), pp. 4936–4948.
653 doi: 10.1088/0004-6256/137/6/4936.

654 Massironi, M., Cremonese, G., Marchi, S., Martellato, E., Mottola, S. and Wagner, R. J.
655 (2009) 'Mercury's geochronology revised by applying Model Production Function to Mariner
656 10 data: Geological implications', *Geophysical Research Letters*, 36(21), p. L21204. doi:
657 10.1029/2009GL040353.

658 Melosh, H. J. (2011) *Planetary Surface Processes*. 1st edn. Cambridge: Cambridge University
659 Press.

660 Melosh, H. J. and Dzurisin, D. (1978) ‘Mercurian Global Tectonics : A Consequence of Tidal
661 Despinning ?’, *Icarus*, 35, pp. 227–236.

662 Melosh, H. J. and McKinnon, W. B. (1988) ‘The Tectonics of Mercury’, pp. 374–400.

663 Pechmann, J. B. and Melosh, H. J. (1979) ‘Global fracture patterns of a despun planet:
664 Application to Mercury’, *Icarus*, 38(2), pp. 243–250. doi: 10.1016/0019-1035(79)90181-7.

665 Preusker, F., Oberst, J., Head, J. W., Watters, T. R., Robinson, M. S., Zuber, M. T. and
666 Solomon, S. C. (2011) ‘Stereo topographic models of Mercury after three MESSENGER
667 flybys’, *Planetary and Space Science*, 59(15), pp. 1910–1917. doi: 10.1016/j.pss.2011.07.005.

668 Prockter, L. M., Ernst, C. M., Denevi, B. W., Chapman, C. R., Head, J. W., Fassett, C. I.,
669 Merline, W. J., Solomon, S. C., Watters, T. R., Strom, R. G., Cremonese, G., Marchi, S. and
670 Massironi, M. (2010) ‘Evidence for young volcanism on Mercury from the third MESSENGER
671 flyby.’, *Science (New York, N.Y.)*, 329(5992), pp. 668–71. doi: 10.1126/science.1188186.

672 Rothery, D. . and Massironi, M. (2013) ‘A spectrum of tectonised basin edges on Mercury’,
673 *LPSC 44*, 1175.

674 Rothery, D. A. and Massironi, M. (2010) ‘Beagle Rupes – Evidence for a basal decollement of
675 regional extent in Mercury’s lithosphere’, *Icarus*. Elsevier Inc., 209(1), pp. 256–261. doi:
676 10.1016/j.icarus.2009.12.009.

677 Solomon, S. C. (2011) ‘A new look at the planet Mercury’, *Physics Today*, 64(1), p. 50. doi:
678 10.1063/1.3541945.

679 Spudis, P. D. and Guest, J. E. (1988) ‘Stratigraphy and geologic history of Mercury’, *Mercury*
680 *University of Arizona Press*, 1, pp. 118–164. Available at:
681 http://adsabs.harvard.edu/abs/1988merc.book..118S.

682 Strom, R. G. and Neukum, G. (1988) ‘10. The Cratering Record on Mercury and the Origin of
683 Impacting Objects’, *Mercury*, pp. 336–373. doi: 10.1103/PhysRevB.53.15485.

684 Strom, R. G., Trask, N. J. and Guest, J. E. (1975) ‘Tectonism and volcanism on Mercury’,
685 *Journal of Geophysical Research*, 80(17), pp. 2478–2507. doi: 10.1029/JB080i017p02478.

686 Watters, T. R. (2004) ‘Thrust faults and the global contraction of Mercury’, *Geophysical*
687 *Research Letters*, 31(4), p. L04701. doi: 10.1029/2003GL019171.

688 Watters, T. R., Cook, a. C. and Robinson, M. S. (2001) 'Large-scale lobate scarps in the
689 southern hemisphere of Mercury', *Planetary and Space Science*, 49(14–15), pp. 1523–1530.
690 doi: 10.1016/S0032-0633(01)00090-3.

691 Watters, T. R., Schultz, R. A., Robinson, M. S. and Cook, A. C. (2002) 'The mechanical and
692 thermal structure of Mercury ' s early lithosphere', *Geophysical Research Letters*, 29(11), pp.
693 1–4.

694 Watters, T. R., Selvans, M. M., Banks, M. E., Hauck II, S. A., Becker, K. J. and Robinson, M. S.
695 (2015) 'Distribution of large-scale contractional tectonic landforms on Mercury: Implications
696 for the Origin of Global Stresses', *Geophysical Research Letters*, 42, pp. 3755–3763. doi:
697 10.1002/2015GL063570.

698 Zoback, M. D., Townend, J. and Grollimund, B. (2002) 'Steady-State Failure Equilibrium and
699 Deformation of Intraplate Lithosphere', *International Geology Review*, 44(5), pp. 383–401.
700 doi: 10.2747/0020-6814.44.5.383.

701

702

Supplementary Information

MPF plots for the model ages presented in Table 2.

SI1: Basins with basin-edge scarps.

SI1a : Marchi et al. (2009) MPF plot for the smooth plains unit (black) and basin-edge scarp (red) of Aneirin.

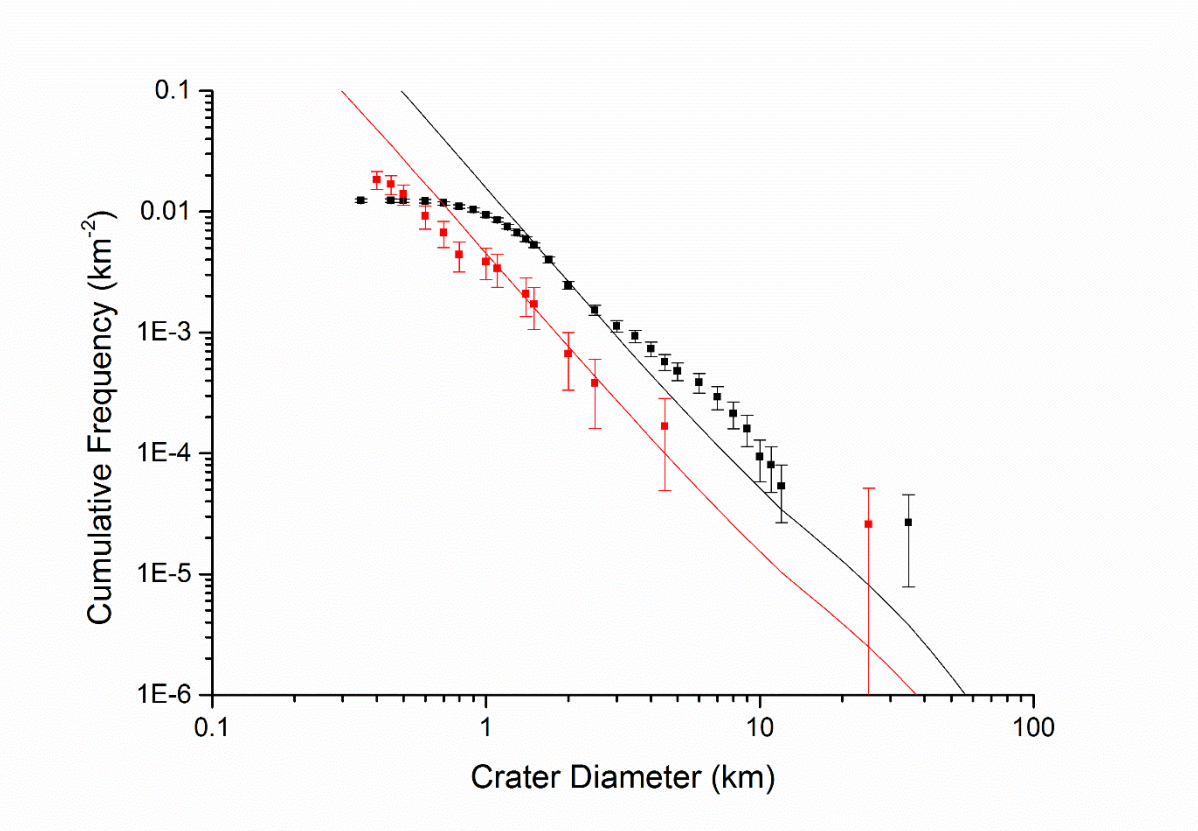

SI1b : Marchi et al. (2009) MPF plot for the smooth plains unit (black) and basin-edge scarp (red) of Beethoven.

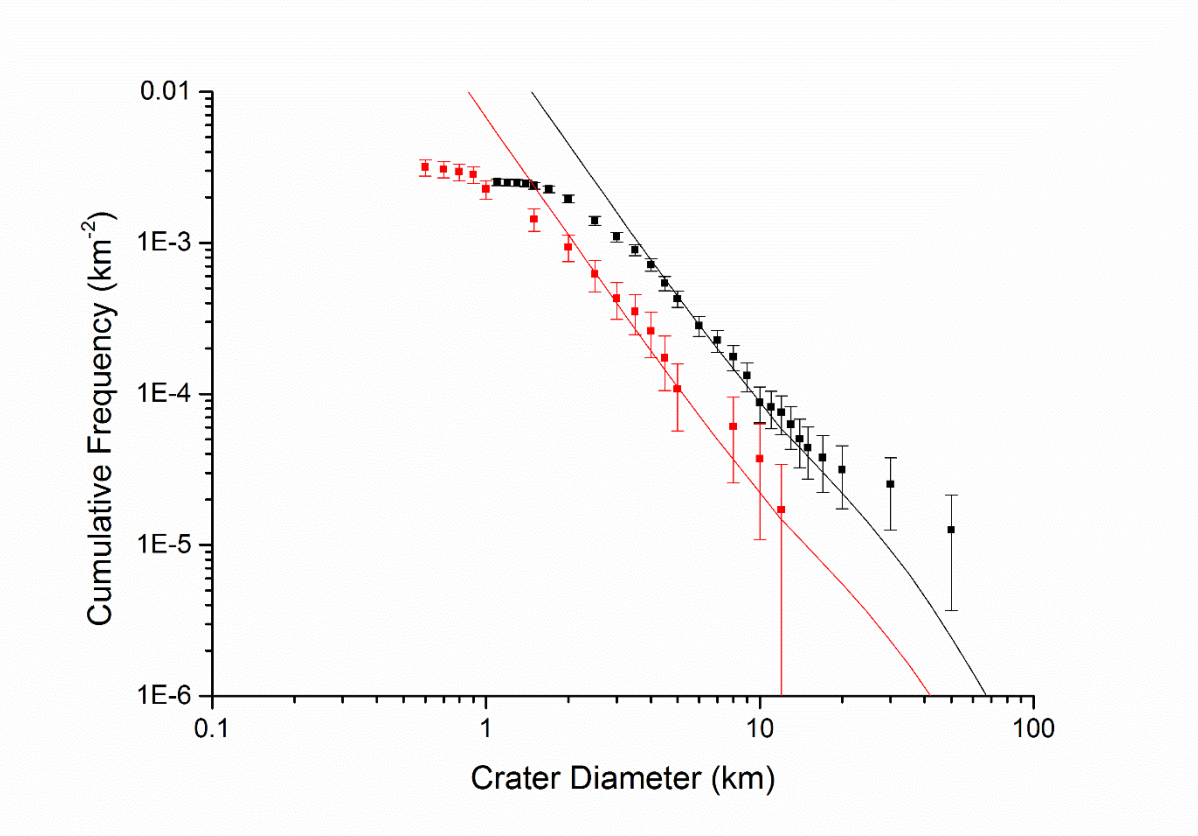

SI1c: Marchi et al. (2009) MPF plot for the smooth plains unit (black) and basin-edge scarp (red) of Hafiz.

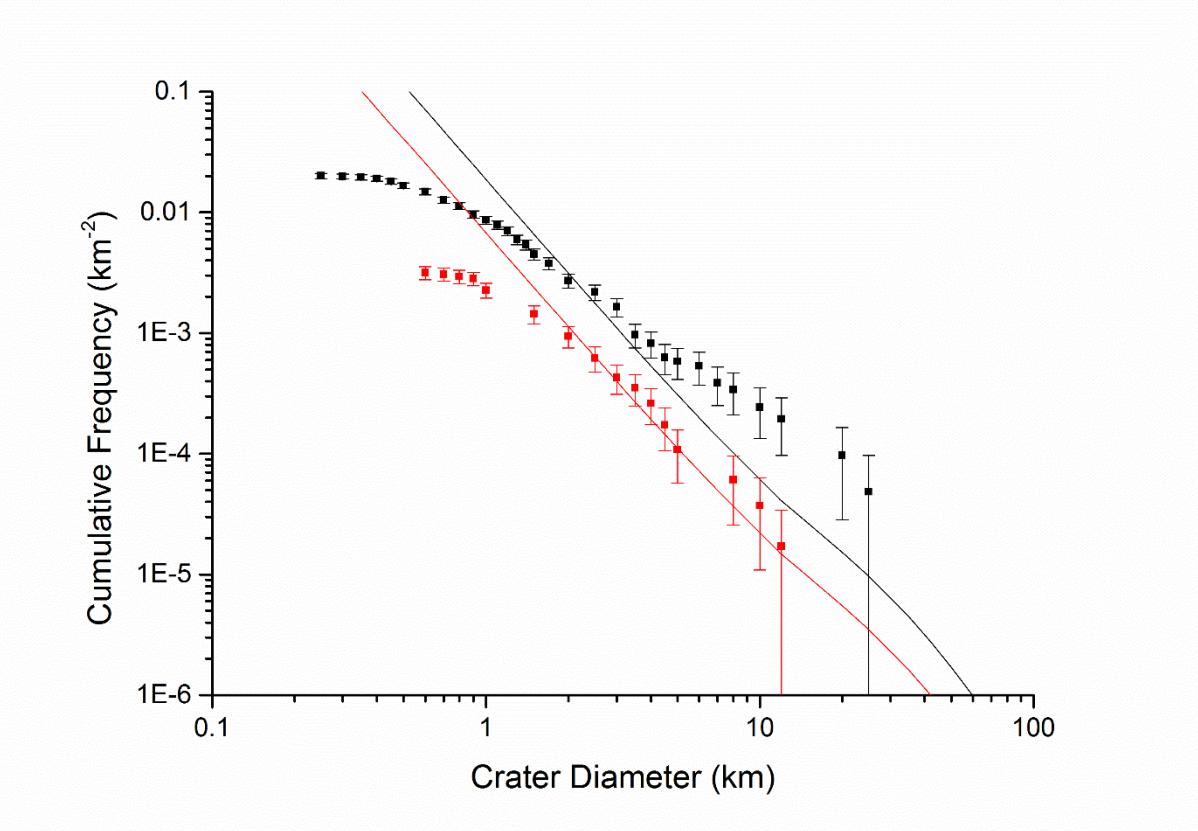

SI1d: Marchi et al. (2009) MPF plot for the smooth plains unit (black) and basin-edge scarp (red) of Shevchenko.

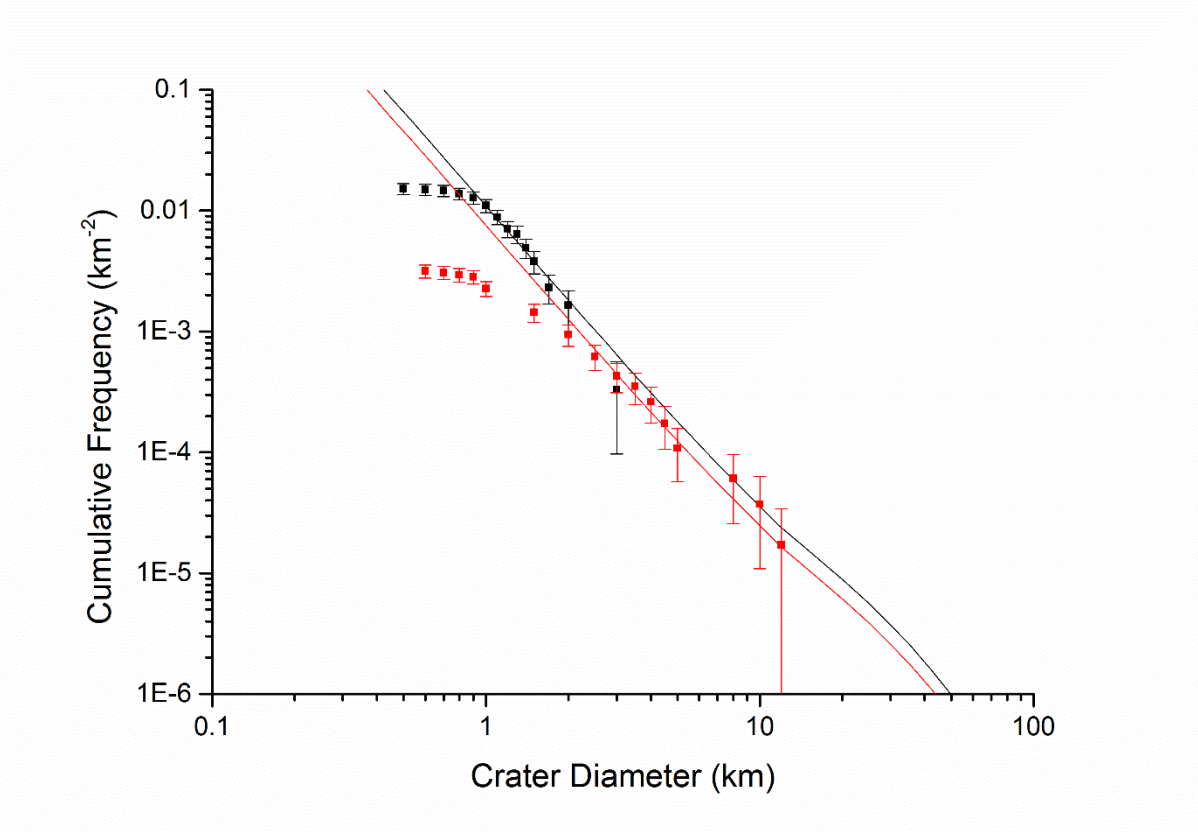

SI1e: Marchi et al. (2009) MPF plot for the smooth plains unit (black) and basin-edge scarp (red) of Unnamed[-40, -70].

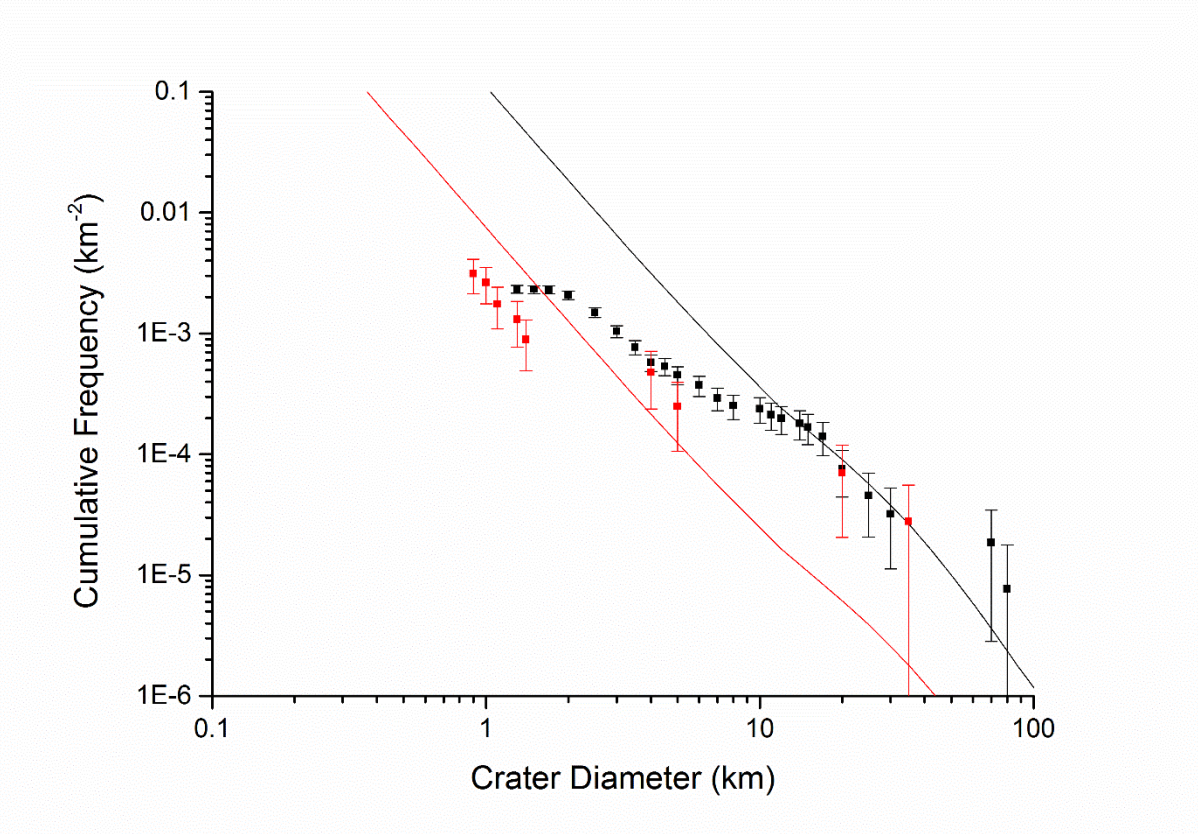

SI1f: Marchi et al. (2009) MPF plot for the smooth plains unit (black) and basin-edge scarp (red) of Unnamed[91, 38].

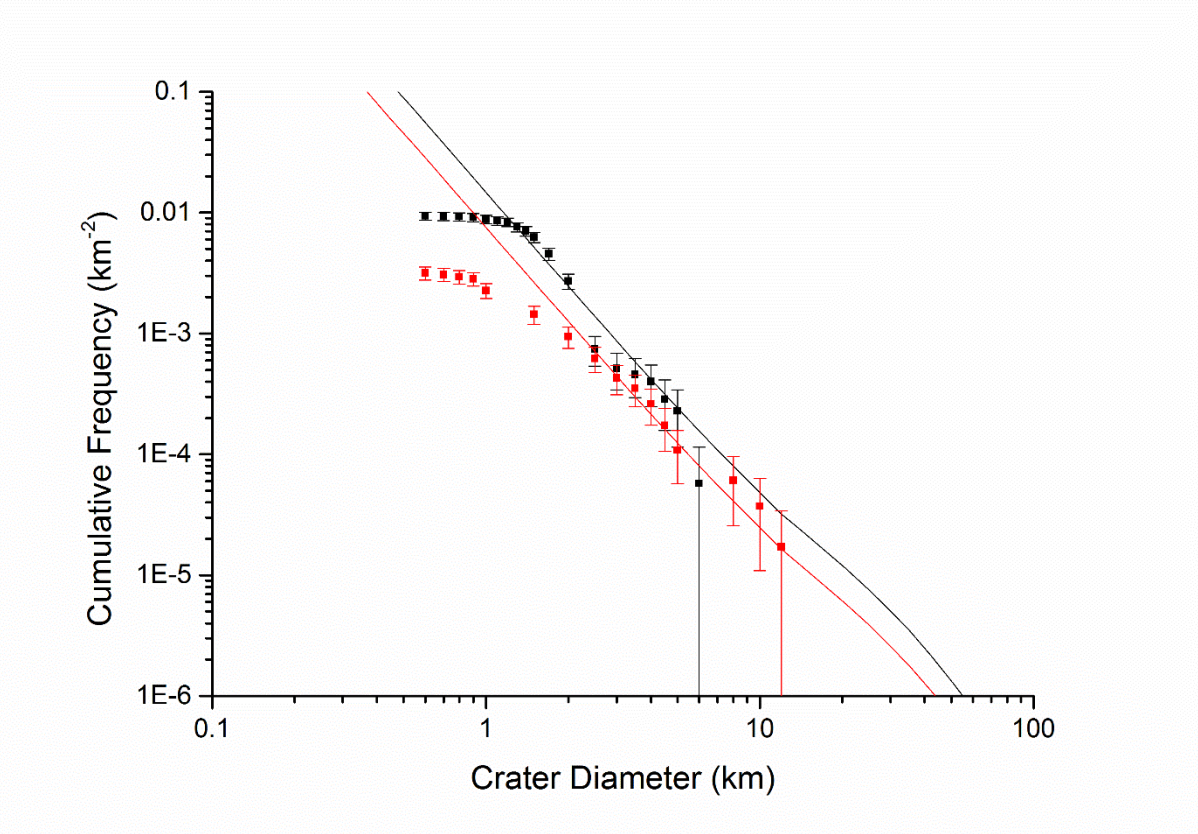

SI1g: Marchi et al. (2009) MPF plot for the smooth plains unit (black) and basin-edge scarp (red) of Unnamed[150, -10].

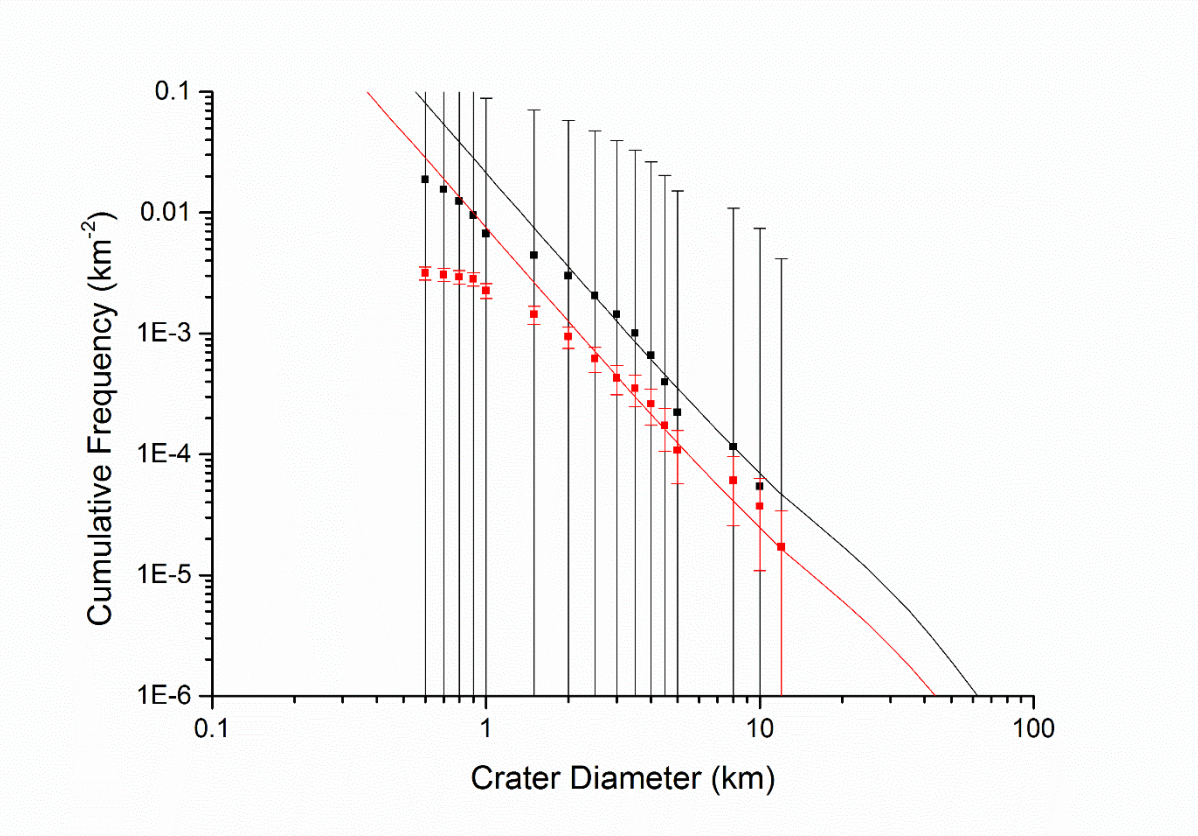

Supplementary Information 2: Basins without basin-edge scarps.

SI2a: Marchi et al. (2009) MPF plot for the smooth plains unit of Mendelson.

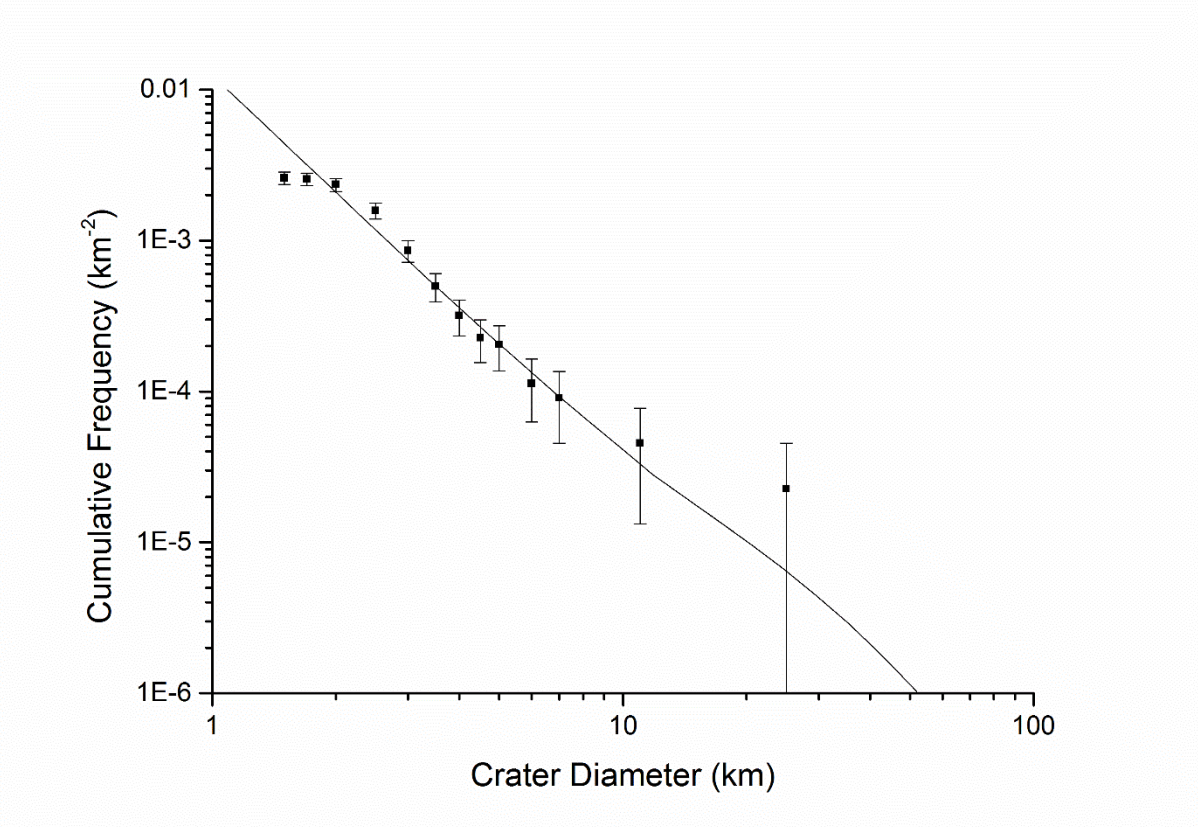

SI2b: Marchi et al. (2009) MPF plot for the smooth plains unit of Hugo.

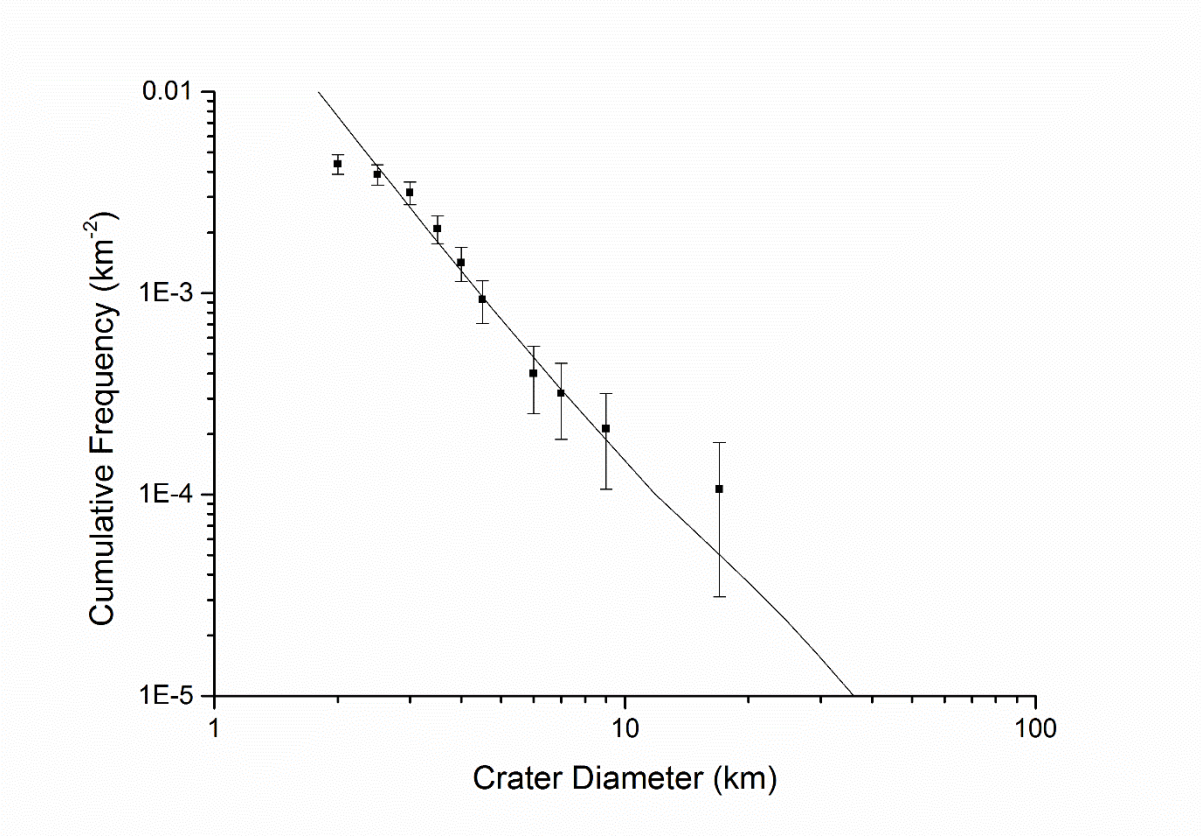

SI2c: Marchi et al. (2009) MPF plot for the smooth plains unit of Khansa.

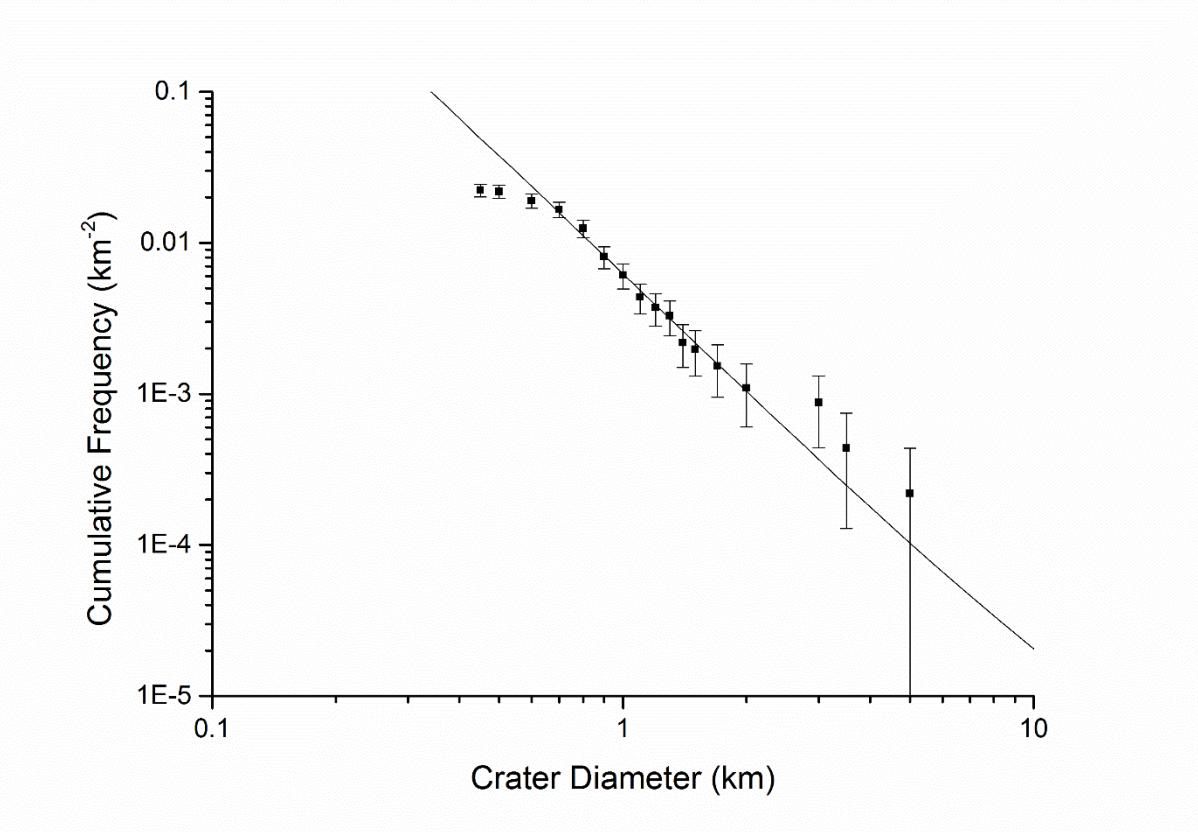

SI2d: Marchi et al. (2009) MPF plot for the smooth plains unit of Copland.

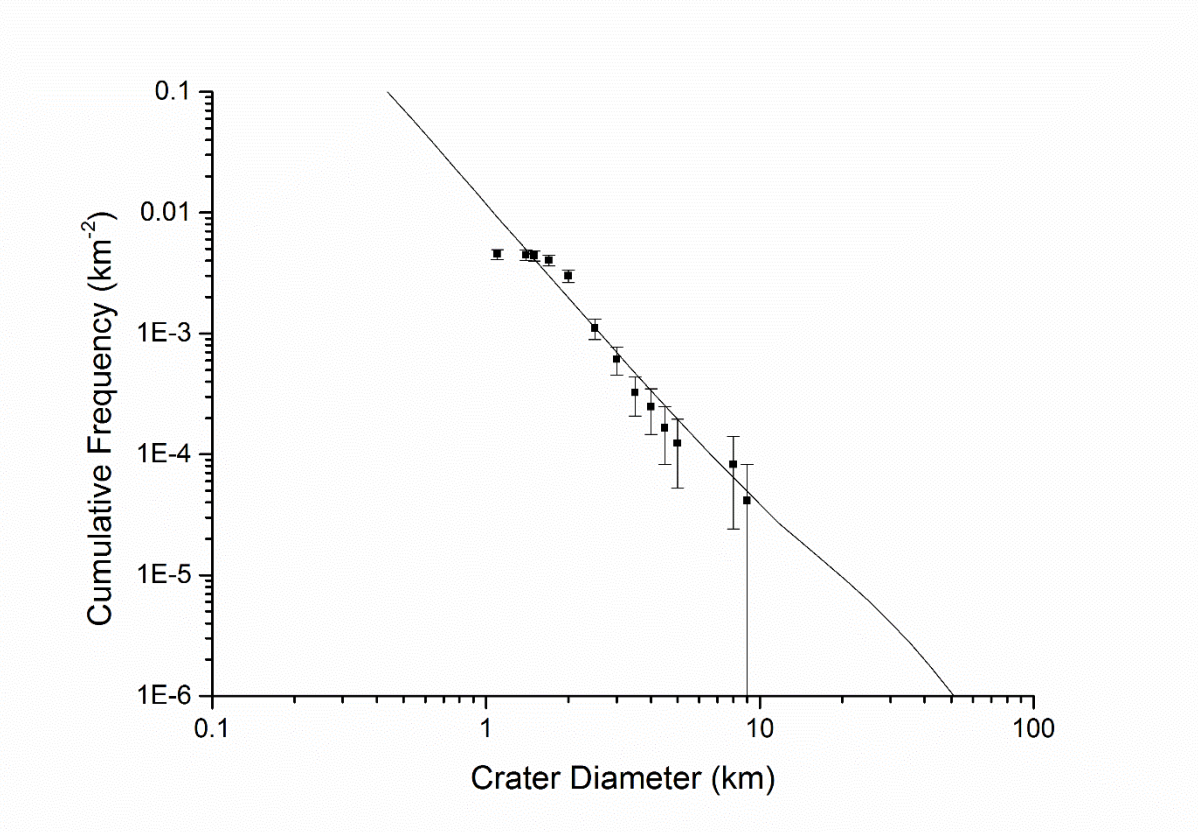

SI2e: Marchi et al. (2009) MPF plot for the smooth plains unit of Unnamed[-166,-25].

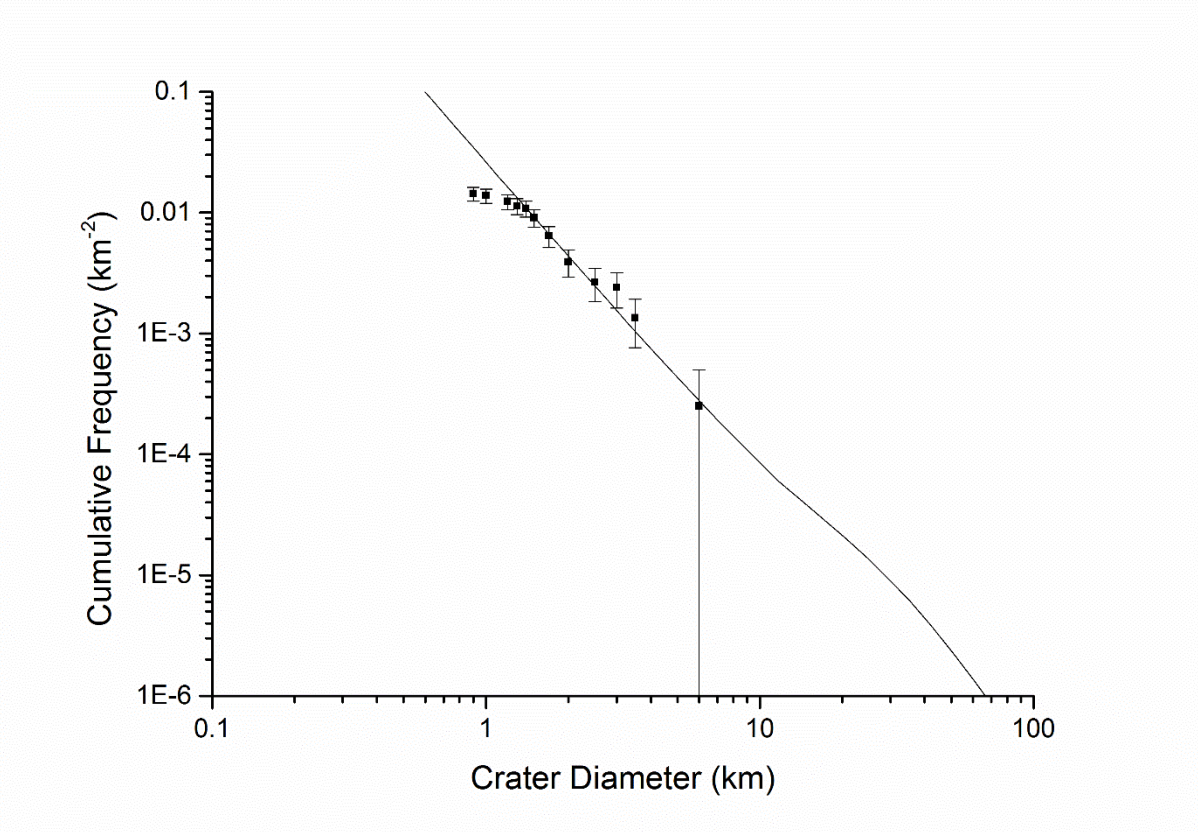

SI2f: Marchi et al. (2009) MPF plot for the smooth plains unit of Unnamed[154,67].

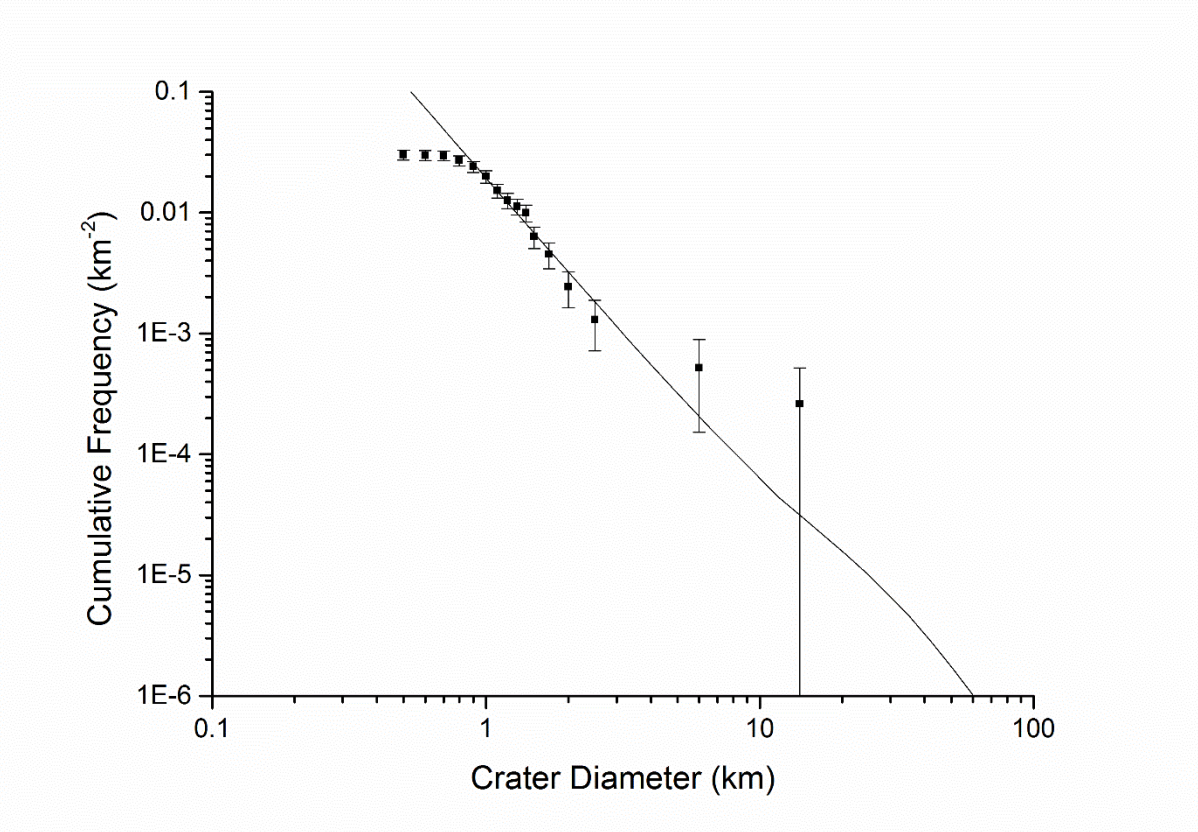

SI2g: Marchi et al. (2009) MPF plot for the smooth plains unit of Unnamed[-69,0].

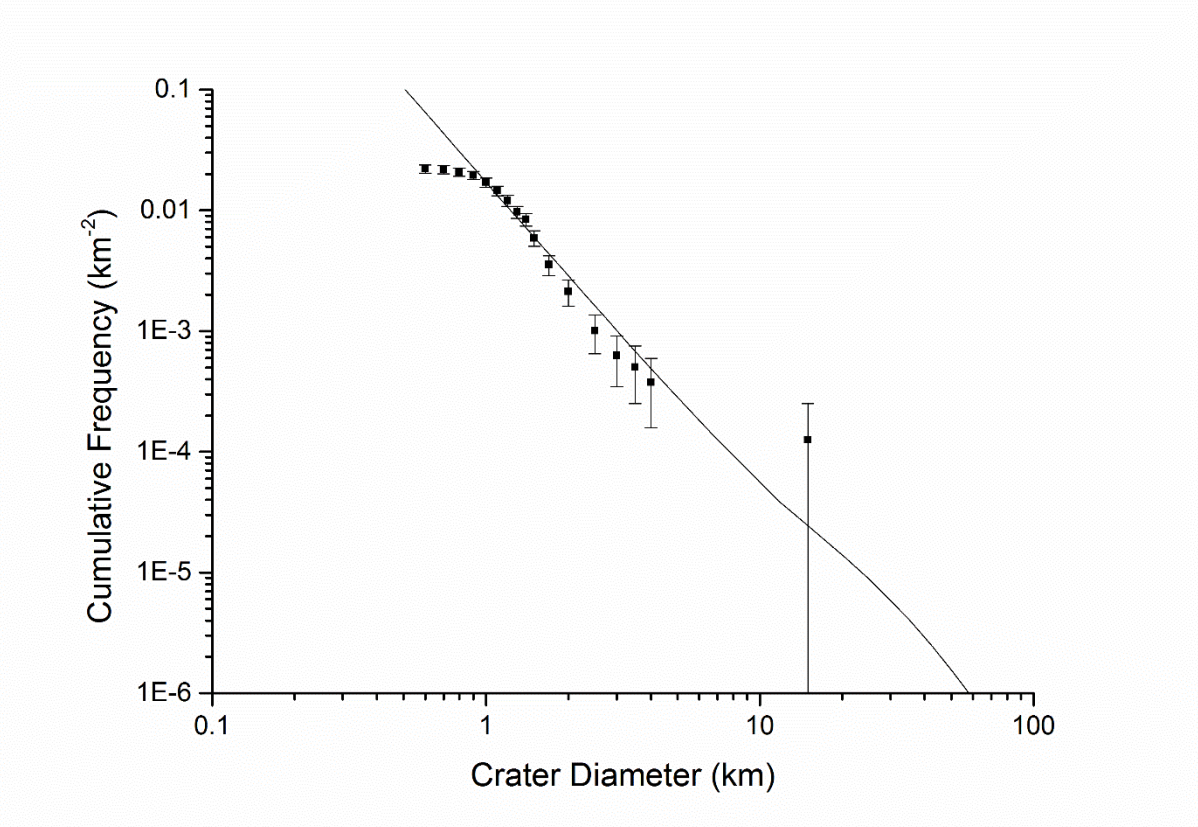

SI2h: Marchi et al. (2009) MPF plot for the smooth plains unit of Unnamed[-13,-22].